A Monte Carlo approach to approximating the effects of pore geometry on the phase behavior of soil freezing

Jiangzhi Chen[1,2], Shenghua Mei[1], Julia T. Irizarry[3], Alan W. Rempel[4]

[1]Institute of Deep-Sea Science and Engineering, Chinese Academy of Sciences, Sanya, Hainan Province, 572000, China

[2]CAS Key Laboratory for Experimental Study under Deep-sea Extreme Conditions, Institute of Deep-sea Science and Engineering, Chinese Academy of Sciences, Sanya, Hainan Province, China

[3]McMillen Jacobs Associates, 1500 SW 1st Ave., Portland, OR 97201, USA

[4]Department of Earth Sciences, University of Oregon, Eugene, OR 97403, USA

Key Points:

- we develop numerical models to evaluate pore geometric constraints on soil freezing with temperature
- our method is validated by comparing modeled results against empirical data and field observations
- soil freezing curves are predicted for log-normal particle-packings in pure and salt-doped systems

Corresponding author: Jiangzhi Chen, chenjz@idsse.ac.cn

Abstract

Freezing in porous media is associated with a host of dynamic phenomena that stem from the presence and mobility of premelted liquid at subzero temperatures. Accurate assessments of the progressive liquid—ice phase transition is required for predictive models of frost damage, glacier—till coupling, and many other cold regions processes, as well as for evaluating the capacity for water storage in near-surface extraterrestrial environments. We use a Monte Carlo approach to sample the pore space in a synthetic 3D packing of poly-dispersed spherical particles, and evaluate local geometrical constraints that allow us to assess changes in the relative proportions of pore fluid and ice. By approximating the phase boundary geometry in fine-grained pores while considering both the curvature of the liquid—ice interface and wetting interactions with matrix particles, our model predicts changes in phase equilibrium in granular media over a broad temperature range, where present accounting for the colligative effects of chloride and perchlorate solutes. In addition to formulating the constitutive behavior needed to better understand properties and processes in frozen soils, our results also provide insight into other aspects of phase equilibria in porous media, including the formation of methane hydrates in permafrost and marine sediments, and the partitioning between liquid water and vapor in the vadose zone.

Plain Language Summary

When saturated soils become frozen at subzero temperatures, the water between the soil grains turns into ice. The soil freezing curves (SFCs) describe how amount of water remaining liquid in pore spaces changes with temperature, which is also determined by the geometry of pores. Previous researches tend to idealize the pores as spheres or cylinders, but the actual pores have irregular geometry, and the interface between water and ice can be so curved that liquid water may exist at temperatures much lower than bulk freezing point. To quantitatively assess the relation between the undercooling and residual liquid water in frozen soils, we construct synthetic soil models with packed spherical particles, and use a Monte Carlo approach to track the ice—liquid interface over a large temperature range. The soil particles can be of a uniform size and following a log-normal size distribution, and the results are compared with ice-infiltration experiments, field observation, and mercury intrusion measurements. Additional factors including the

wetting of ice and dissolved salts are also taken into account. The model can shed light on the formation of ice and gas hydrate in permafrost and extraterrestrial systems.

1 Introduction

In open systems, equilibrium between pure liquid water and ice takes place at a bulk melting temperature that depends only on the pressure to which both phases are subject. However, in fine-grained porous media the effects of surface energy and intermolecular interactions involving matrix surfaces cause the pressure in the ice to differ from the pressure in the liquid along their mutual interface. The phenomenon of premelting describes the resulting equilibrium phase coexistence, which can take place over a broad range of temperatures as the interface geometry changes (e.g., Dash et al., 2006, and others). Soil freezing curves (SFCs) describe how the fraction of the pore space inhabited by liquid is reduced as cooling increases the size of the departure beneath the bulk melting temperature (e.g., Cahn et al., 1992; Orlando B. Andersland, 2003; Hansen-Goos & Wettlaufer, 2010). This mobile liquid phase plays a central role in diverse processes, including frost damage to cohesive materials (e.g., Hallet et al., 1991; A. W. Rempel et al., 2016; A. W. Rempel & Rempel, 2019), frost heave in unconsolidated sediments (e.g., A. W. Rempel, 2010; Sizemore et al., 2015), and glacier sliding (Meyer et al., 2018; Lipovsky et al., 2019). Moreover, similar perturbations to phase equilibria between pore constituents are important in other systems, for example leading to the development of gas hydrate anomalies in submarine sediments (e.g., A. W. Rempel, 2011; Handwerger et al., 2017; VanderBeek & Rempel, 2018), determining the partitioning between liquid water and air in porous materials (e.g., Or & Hanks, 1992; Or & Tuller, 1999; A. Rempel & Rempel, 2016), and facilitating salt damage to the built environment (e.g., Scherer, 1999).

As illustrated in Figure 1, porous-media induced shifts from bulk equilibrium have two primary causes: (1) the confined geometry forces the ice—liquid interface to curve, thereby enhancing the area and energy of the bounding surface that encompasses a given ice volume; (2) the intermolecular forces between particle surfaces, liquid, and ice induce liquid films to wet the interfaces between soil particles and ice crystals. As a result of these pore-scale effects, the equilibrium ice—liquid temperature in the residual liquid depends on the volume fraction of the pore space that it occupies, referred to here as the liquid saturation S_l, enabling residual liquid to remain in equilibrium at a saturation level that depends on the undercooling $\Delta T = T_m - T$, defined as the temperature depres-

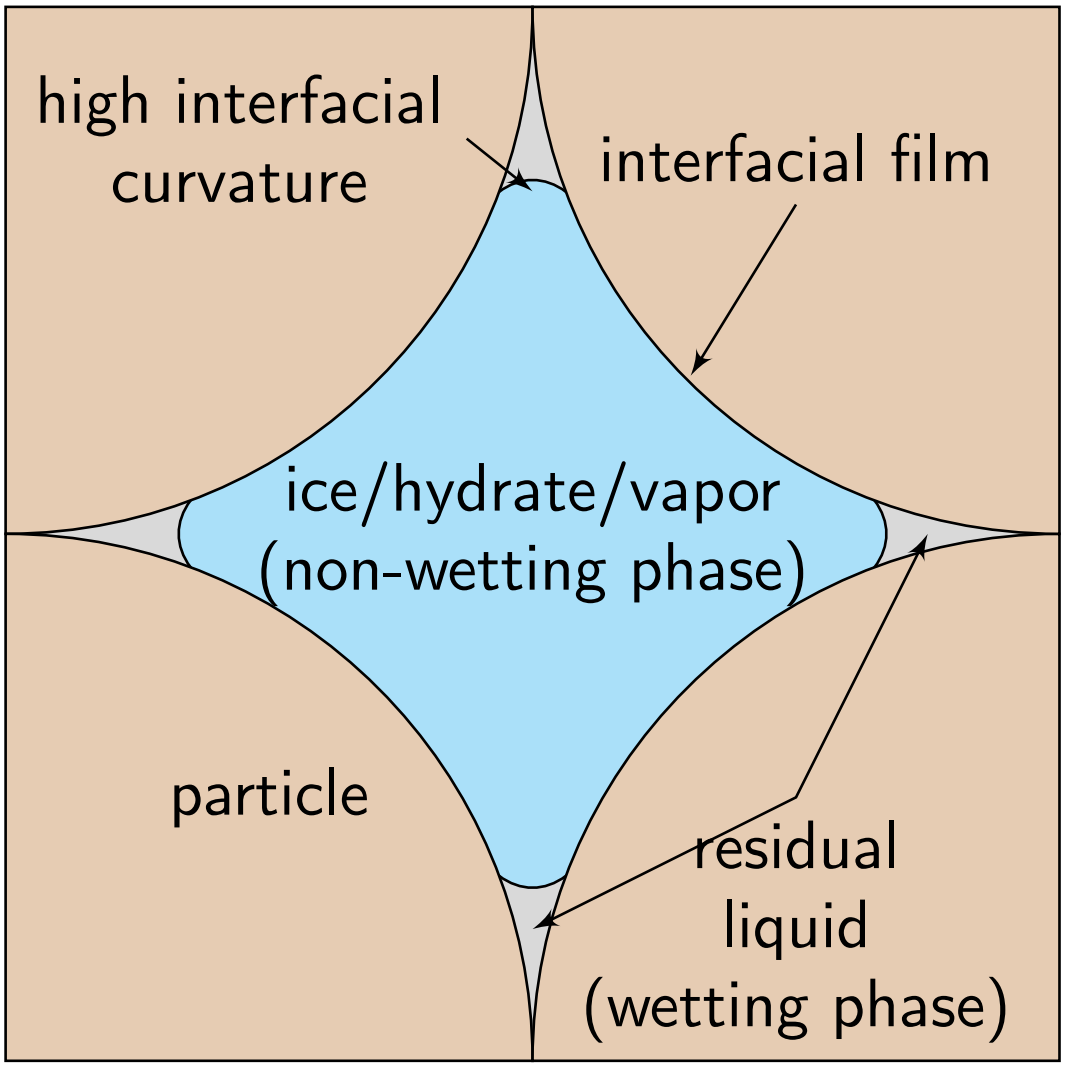

Figure 1. Schematic diagram showing the configuration of a non-wetting phase, such as ice (or vapor), surrounded by a residual liquid phase that wets the particle surfaces bounding an idealized pore. Liquid remains in equilibrium near particle contacts where the curvature of the ice—liquid interface is high (i.e., the radius of curvature is small). These tiny reservoirs are connected by thin liquid films that coat the particle—ice interface.

sion below the normal bulk melting point T_m (e.g., Dash et al., 2006). Analogous behavior occurs in vapor—water—particle systems, where the liquid saturation depends on the matric potential, which is the pressure difference between the non-wetting vapor phase and the wetting liquid phase (e.g., Or & Tuller, 1999). Here, we demonstrate a computational method based on Monte Carlo techniques that quantifies shifts to the equilibrium phase behavior in porous media modeled using randomly packed, poly-dispersed spherical particles. Below, we describe our approach, model validation tests, and the implications of our results for frozen soils, both with and without the presence of other soluble impurities (e.g., deicing salt, mostly $MgCl_2$) that are assumed to be completely excluded from the crystalline ice structure. Moving beyond terrestrial applications, the detection of perchlorate salts and shallow subsurface ice deposits at the Phoenix lander site (Hecht et al., 2009) motivate an illustration of the influence of these salts on the residual liquid fraction in equilibrium with ice in the Martian regolith.

Several phenomenological models have been developed to demonstrate how pore-scale effects produce shifts to the phase behavior in porous media. Many approximate pores as circular cylinders (e.g., Denoyel & Pellenq, 2002), others employ spherical pores connected by cylindrical pore throats (e.g., Jang & Santamarina, 2011), cylindrical pores of triangular cross-section (A. W. Rempel, 2011), and two-dimensional pores bounded by circular particles (A. W. Rempel, 2012). Although useful for many purposes, these idealizations are unable to capture several notable aspects of phase boundaries in natural porous media. For example, as suggested by the illustration in Figure 1, the liquid saturation level in a given pore can vary continuously over a broad range of values as the curvature of the phase boundary near particle contacts changes; circular and cylindrical pore geometries admit only a single curvature value (2/radius and 1/radius, respectively) so that liquid saturation within a given pore can vary only to the limited extent allowed by changes in film thickness. Pores of triangular cross-section allow for curvature variations, but unlike natural porous media they incorporate no regions of negative interfacial curvature (i.e., where the center of curvature is outside of the non-wetting phase, like in the film regions of Figure 1). Furthermore, realistic models of interface geometry require three-dimensional treatments that allow for finite differences between the two principal radii of curvature (one of which is infinite in idealizations that employ cylindrical geometries). Fully capturing the three-dimensional geometry of the phase boundary is an intricate problem, even for porous media characterized by idealized packings

of equal-sized spheres (see e.g., Cahn et al., 1992). However, progress can be made without evaluating the entire geometry of the phase boundary, but instead sampling the pore space at discrete points and approximating only the local geometry of the phase boundary as it first encompasses each sampled location. This approach was taken by A. W. Rempel (2012) in two-dimensional calculations; here we extend the treatment to three dimensions in a synthetic porous medium comprised of poly-dispersed spherical particles.

The paper is organized as follows: section 2 gives a brief overview of the basic geometrical controls on phase equilibria in porous media, section 3 describes our procedure for producing SFCs in synthetic porous media formed from random packings of spherical particles, section 4 summarizes several model validation tests and illustrates predicted SFCs in pure and impurity-doped water for porous media formed from log-normally distributed particle assemblages, section 5 discusses the implications of our results before concluding remarks are provided in section 6.

2 Phase behavior in porous media

The geometry of the phase boundary at different saturation levels can be described in terms of its varying interfacial mean curvature $\mathcal{K}$ and separation d from particle surfaces; these geometrical parameters can also be used to describe the perturbations to the phase behavior within the porous medium. The surface energy of the water—ice phase boundary $\gamma \approx 0.029\,\mathrm{J/m^2}$ (Hardy, 1977) and the intermolecular forces that produce wetting films both result in an offset between the pressures in the non-wetting P_{nw} and wetting P_l (assumed here to be liquid) phases. Together, these effects can be combined to write

$$P_{nw} - P_l = \gamma\mathcal{K} + P_T, \tag{1}$$

where $P_T(d)$ describes how the "disjoining pressure" associated with wetting interactions increases as the film thickness d shrinks, and we define $\mathcal{K}$ in terms of two principal radii of curvature r_1 and r_2 so that $\mathcal{K} = 1/r_1 + 1/r_2$. In the vadose zone, where the non-wetting phase is air, eq. (1) describes the geometrical controls on how the so-called "liquid retention curve" varies as a function of the matric potential $P_{nw} - P_l$. When the phase boundary can be crossed through melting, as with pores containing liquid water and ice, the generalized Clapeyron equation can be used to substitute for the pressure difference on the left side of eq. (1) and find that the depression of the temperature T

below the bulk melting temperature T_m at reference pressure P_m satisfies

$$\frac{\rho_{nw} L(T_m - T)}{T_m} + (P_m - P_l)\left(1 - \frac{\rho_{nw}}{\rho_l}\right) \approx \frac{\rho_{nw} L(T_m - T)}{T_m} = \gamma\mathcal{K} + P_T, \tag{2}$$

where ρ_{nw} and ρ_l are the densities of the non-wetting solid phase and wetting liquid phase, and L is the latent heat of fusion. Because the densities of water and ice are within 10% of each other, for variations in the liquid pressure encountered in nature, typically the second term on the left side of eq. (2) is negligible. We note that eq. (2) is a generalized form of the Gibbs-Thomson relation with an additional term P_T that becomes significant as the phase boundary approaches pore walls.

We treat the surface energy γ as constant in all of our calculations, so the main challenge in evaluating the first term on the right sides of eqs. (1) and (2) comes from determining $\mathcal{K}$. In contrast, the distance d to the nearest particle is easily obtained, but in nature the dependence of P_T on d is sensitive to properties of the ice and particle surfaces (including surface charge), as well as such subtleties as the distribution of ions in the residual liquid. Israelachvili (2011) provides a comprehensive discussion of the controls on wetting behavior that determine how exactly the film thickness d decreases as P_T is enhanced. Hansen-Goos and Wettlaufer (2010) highlight the complexities of variations in liquid film thickness during ice formation in mono-dispersed random close-packed spheres, focusing their attention on conditions in which the residual liquid saturation is low enough that its volume is dominated by the films, rather than by the small reservoirs near particle contacts that are controlled primarily by the effects of high interfacial curvature (see Figure 1). Here, our interest in the dynamic interactions that take place when the liquid saturation is relatively high, so that water mobility is appreciable, leads us to focus primarily on the regime in which high-curvature reservoirs hold much more liquid than the films that coat particle surfaces. Accordingly, we avoid introducing unnecessary detail in our treatment of films and instead follow previous workers (e.g., Cahn et al., 1992; A. Rempel & Worster, 1999; Tuller & Or, 2005) in approximating the effects of wetting interactions using a simple power law so that

$$P_T \approx P_0\left(\frac{\lambda_0}{d}\right)^b, \tag{3}$$

where the value of b is determined by the dominant microphysical interactions (for illustration below we set $b = 3$), and λ_0 is the film thickness at reference pressure P_0. In our models to follow, we treat λ_0 as an adjustable parameter.

175 ## 3 Models

176 To model the three-dimensional pore geometry, we first simulated a random sphere-
177 packing process in MATLAB following the classical drop-and-roll scheme (e.g., Jodrey
178 & Tory, 1979; Shi & Zhang, 2008), and then used the resulting sphere packs as simulated
179 soils for evaluating the equilibrium phase perturbations. Because the algorithms we use
180 in this work require patience to construct, we provide the MATLAB scripts (Chen & Rem-
181 pel, 2019a, 2019b) under the MIT license. We implement a Monte Carlo routine that sam-
182 ples a large number of random test points within a single plane cutting through the par-
183 ticle pack, detailed in Appendix A1. The presence of additional soluble impurities mod-
184 ifies the equilibrium behavior in a manner that we approximate with slight modifications
185 to this procedure, as described in section 3.6 below.

186 ### 3.1 Scenario 1: Pore ice

187 The first ice to be at equilibrium within a given pore is bounded by the surface with
188 the smallest constant curvature that will fit between the bounding particles. We approx-
189 imate the geometry of such "pore ice" by the largest sphere that will fit within the pore
190 while still containing a particular test point, as illustrated in Figure 2a. We arrive at this
191 estimate through an iterative process, detailed in Appendix A2. The phase perturba-
192 tion that would be required to place the point within our approximation for the first ice
193 crystal of a radius r_p that could attain equilibrium within the pore can be written by
194 setting $P_T \approx 0$ and $\mathcal{K} \approx 2/r_p$ in eqs. (1) and (2) so that

195 $$P_{nw} - P_l \approx \frac{\rho_{nw} L}{T_m} (T_m - T) \approx \frac{2\gamma}{r_p}. \tag{4}$$

196 ### 3.2 Scenario 2: Throat ice

197 Points near to the pore throats that constitute the connections between adjacent
198 pores are often outside the region spanned by the first pore ice crystal, and are instead
199 referred to here as "throat ice". The ice interface first intersects a test point in a pore
200 throat when its surface geometry has the smallest curvature possible while remaining tan-
201 gent to the pair of particles that spans the throat (see Figure 2b). To approximate the
202 constant curvature surface in this scenario, we seek the radius r_t of the hemispherical
203 cap that satisfies these geometrical constraints.

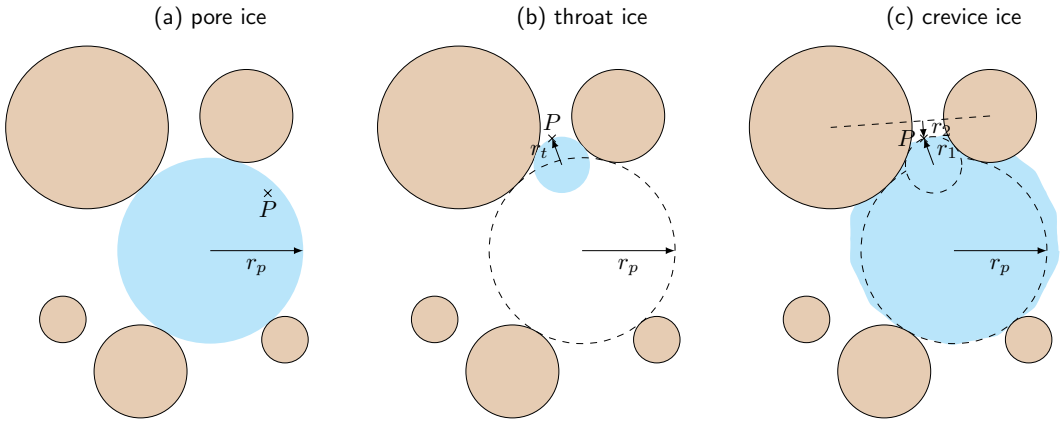

Figure 2. Schematic diagrams showing a cross-section through a 3D porous medium. A test point is indicated with an asterisk in each panel. (a) The test point is located within a closed surface of constant curvature that is approximated using the largest sphere (radius r_p) to encompass the point while fitting within the pore. (b) The test point is outside of the region where the non-wetting phase is first stable (bounded by the dashed circle), but instead lies upon the phase boundary formed in part by a hemispherical protrusion that extends into the pore "throat" between the two nearest particles. (c) The test point lies in a "crevice" region between two particles on a constant-curvature surface of revolution about the dashed line (e.g., an unduloid) that is approximated as having positive principal radius of curvature r_1 and negative principal radius of curvature r_2. At this stage, the entire non-wetting phase has extended beyond the pore region defined by the largest inscribed sphere. For illustration in this 2D plot we show the spherical particles as coplanar with the ice and the test point, but our numerical procedure is not limited by this idealization.

Due to symmetry, the center of the largest hemispherical cap is coplanar with the centers of the two tangent particles and the test point. In this plane we find the "Apollonius" circle tangent to the two particles (projected as circles) and the test point (Coxeter, 1968), which leads to a second estimate for the phase perturbation at the test point, again satisfying eq. (4), but with $r = r_t$. We note that by approximating the constant curvature surface as a hemispherical cap, we obtain a conservative estimate for the phase perturbation at which ice can first intersect such test points, since in reality the second principle radius of curvature may be larger and so lead to a curvature that is lower than the assumed value of $\mathcal{K} = 2/r_t$. In the results presented below we provide two separate estimates of the changes in liquid saturation with increasing perturbation from bulk equilibrium: in the case we refer to as the "throat total" liquid saturation, we assume that any phase boundary that encounters a test point far from particle surfaces has a curvature that can be approximated using a hemispherical cap; in the case we refer to as the "crevice total" liquid saturation, we assume instead that the phase boundary at such locations is better described by two distinct radii of curvature with opposite signs, as described next.

3.3 Scenario 3: Crevice ice

Near the contact between two particles, residual liquid can remain until "crevice ice" impinges, as illustrated in Figure 2c. The unduloid interface between the crevice ice and residual liquid is approximated as part of a torus (Fisher, 1926), as detailed in Appendix A3. We again follow Apollonius in determining the two principle radii of curvature r_1 and $-r_2$, as shown in Figure 2c. In this case, the stable liquid—ice interface is a concave meniscus, and the test point must lie within the truncated cone region formed with the common tangent line of the two particles. We set $P_T \approx 0$ and $\mathcal{K} \approx 1/r_1 - 1/r_2$ in eqs. (1) and (2) to estimate the resulting phase perturbation as

$$P_{nw} - P_l \approx \frac{\rho_{nw} L}{T_m} (T_m - T) \approx \gamma \left(\frac{1}{r_1} - \frac{1}{r_2} \right). \tag{5}$$

It is worth noting that the surface construction we use for crevice ices only approximates the constant curvature constraint; a more involved procedure for the construction of so-called "Delaunay surfaces" of revolution that do have constant curvature (e.g., López, 2013) could be pursued, but validation exercises described below suggest that the simpler, approximate treatment outlined here is adequate.

3.4 Scenario 4: Film ice

Test points close to the surface of a particle will remain in the wetting liquid until the perturbation to the phase equilibrium is sufficiently large that the film thickness d matches that separation. Describing the wetting interactions using eq. (3), and assigning the radius of the nearest particle as r, the phase perturbation from eqs. (1) and (2) can be written as

$$P_{nw} - P_l \approx \frac{\rho_{nw} L}{T_m} (T_m - T) \approx P_0 \left(\frac{\lambda_0}{d} \right)^b - \frac{2\gamma}{r}. \tag{6}$$

3.5 Summary of Geometrical Constraints on SFCs

With all the scenarios considered, the modeling algorithm is summarized in Figure 3 as a flowchart. The number of Monte Carlo sampling points is $i_{\max}$. For each test point, first we check whether it is inside a solid particle, and if not, we proceed to evaluate the undercooling for a liquid film, and then find the Apollonius circle. If the test point is inside the truncated cone region, a stable crevice ice is possible and the two principal radii are calculated from the Apollonius circle. No matter whether a crevice ice exists, the throat ice has the Apollonius circle as its great circle, and it must not intersect with any other particles, otherwise we calculate the pore ice that encompasses the test point and touches four particles, or touches three particles and the test point.

3.6 Solutal Effects

The presence of soluble impurities, such as the components of sea salt or perchlorates, modify the phase behavior to a degree that depends on their dissolved concentration in the residual liquid m_s, which is defined here as the solute molarity. Assuming that the impurities are perfectly excluded from the ice lattice, mass balance for the solute requires that m_s be related through S_l to the total bulk concentration $m_b \approx S_l m_s$, which is defined here as the solute content divided by the total volume of pore constituents. When the bulk concentration can be treated as approximately constant, eq. (2) implies that

$$T_m^0 - T \approx \frac{T_m^0}{\rho_{nw} L} (\gamma \mathcal{K} + P_T) + \Gamma \left(\frac{m_b}{S_l} \right), \tag{7}$$

where the superscript 0 denotes the freezing point of pure liquid water, and $\Gamma(m)$ is the undercooling caused by the solute of concentration m, which is explained in detail in Appendix B.

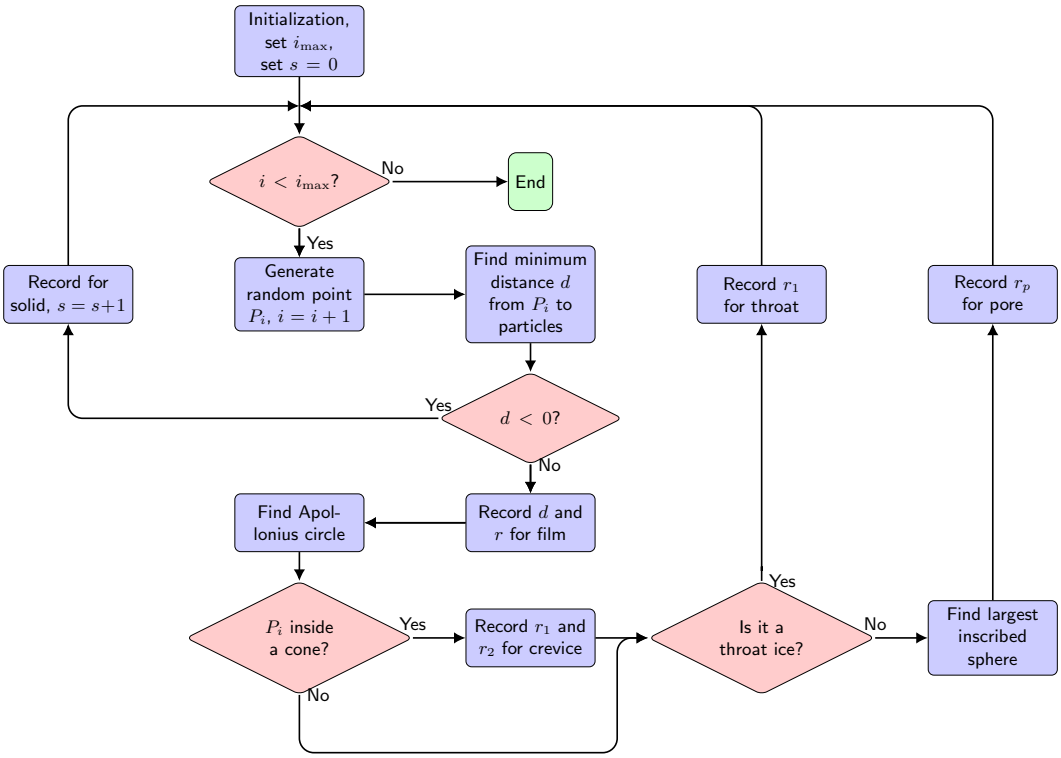

Figure 3. Flowchart of the different scenarios each test point goes through. The conditional nodes are of pink diamond shape, and process nodes are blue rectangles.

4 Validation and Results

To validate our modeling approach we compared predicted phase perturbations to: Sec. 4.1 analytical approximations for simple cubic packing of mono-dispersed spheres; Sec. 4.2 experimental measurements of the changes in liquid saturation with undercooling in two ice-bound porous media; Sec. 4.3 experimental measurements of the changes in liquid saturation with matric potential in a silt loam; and Sec. 4.4 experimental measurements of the changes in liquid saturation inferred from mercury porosimetry on sediments formed from poly-dispersed equant particles. We provide the results of these tests next, before illustrating predicted SFCs in Sec. 4.5. There, we focus on the role of curvature effects in synthetic sediments formed from particles characterized by log-normal size distributions with varying median diameter and skewness, before briefly exploring the influence of wetting behavior, and the presence of soluble impurities.

4.1 Comparison with analytical approximations for simple-cubic packing

Cahn et al. (1992) developed an approximate analytical expression for the equilibrium undercooling $\Delta T = T_m - T$ of ice—liquid mixtures in a simple-cubic packing of identical spheres. Their treatment considers the changes in liquid saturation in both the "crevice" regions described above (see Figure 2c) and the wetting films, which are approximated using eq. (6) (with $b = 3$, $P_0 = 1.1\,\mathrm{MPa}$ and $\lambda_0 = 3.5\,\mathrm{nm}$) while neglecting surface-energy effects (i.e., taking $2\gamma/r \to 0$). For simple-cubic packing of particles with radius r, the pores can encompass spheres of maximum radius $r_p = (\sqrt{3} - 1)r$, implying that the equilibrium configuration switches from complete liquid saturation at warmer temperatures (i.e., $S_l = 1$) to a liquid saturation just under $S_l \approx 0.57$ at an undercooling that can be calculated from eq. (4) as

$$\Delta T = \frac{\gamma T_m}{\rho_{nw} L} \frac{2}{(\sqrt{3} - 1)r} \tag{8}$$

which is approximately $0.071\,\mathrm{K}$ for the ice—water system when the particle radius is $r = 1\,\mu\mathrm{m}$.

Figure 4 illustrates some important features of the predicted phase behavior for this porous medium. Increasing the undercooling from zero, the throat total curve (blue crosses) correctly predicts complete liquid saturation until $\Delta T \approx 0.071\,\mathrm{K}$, before S_l drops abruptly as expected with the first appearance of pore ice. The second kink at $\Delta T \approx 0.124\,\mathrm{K}$ corresponds to another characteristic radius $r_p = (\sqrt{2} - 1)r$: the maximum radius of an ice sphere that is centered on a pore throat, obtained at residual liquid saturation $S_l \approx 0.18$, which is also corroborated by the theoretical predication of the volume occupied by residual liquid (the black dashed curve). By contrast, the analytical approximation by Cahn et al. (1992) erroneously predicts minor ice accumulation at warmer temperatures; this results from the mistaken attribution of a crevice-like geometry (i.e., characterized by two principal radii of curvature with opposite signs) to the phase boundary in pore throats. This problem is corrected in our crevice total prediction (green squares), and the curve agrees well with the red dashed curve, which is the theoretical prediction for the residual liquid volume in crevice regions and films. At large undercoolings, once the liquid saturation falls below about 0.1, the closer correspondence between the crevice total and Cahn et al. (1992) curves can be attributed to a more realistic approximation of the phase behavior in residual high-curvature reservoirs near particle contacts than

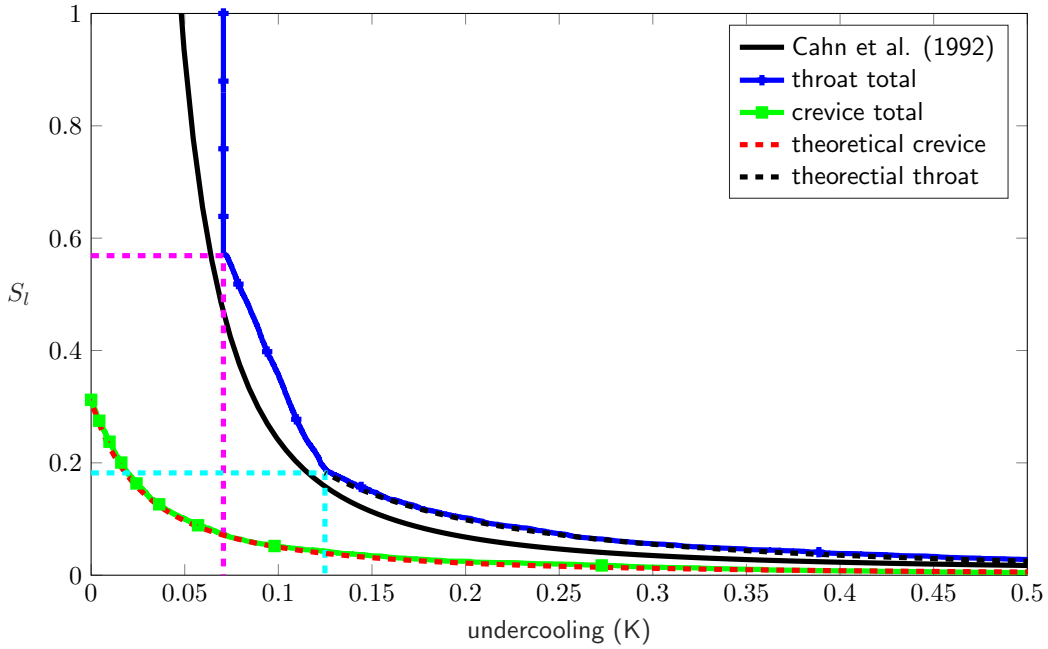

Figure 4. Model predictions for the liquid saturation as a function of undercooling in simple-cubic packing of identical spheres with $r = 1\,\mu m$. The figure shows limiting cases in which, following the appearance of the first pore ice, all curvature-controlled residual liquid is treated as residing in "throats" (blue crosses) and "crevices" (green squares). The solid black curve is the analytical approximation from Cahn et al. (1992). The magenta dashed lines intersect at an abrupt kink in our model curves that takes place at a liquid saturation of 0.57, and undercooling 0.071 K, corresponding with the abrupt appearance of the non-wetting ice phase as the largest spherical crystals that can occupy the available pores, and the cyan dashed lines indicates a second kink at a liquid saturation around 0.18 and undercooling 0.124 K, corresponding to throat ice crystals of radius $(\sqrt{2} - 1)r$. The "throat total" curve captures this feature, and the "crevice total" curve agrees well with the theoretically predicted undercooling (red dashed) caused by ice growing into the particle crevices. In the treatment of Cahn et al. (1992), the volume of liquid in the crevice is approximated to the first order, causing incorrect appearance of a non-wetting phase at warmer temperatures than are possible.

that obtained by the throat total calculations. In this simple example, the throat total curve is more reliable at high liquid saturations and the crevice total curve gives a better approximation to the phase behavior at low liquid saturations. Importantly, the similarity between the two sets of model predictions and the analytical approximation of Cahn et al. (1992) suggests that errors in predicted saturation levels remain small throughout the entire range of undercoolings.

4.2 Comparison with liquid saturation in ice-infiltrated powders

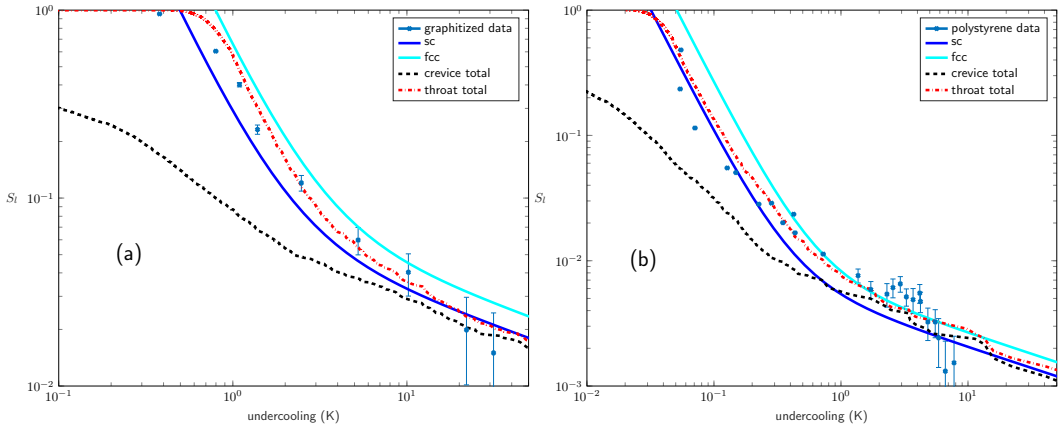

Figure 5. Model predictions and undercooling data from laboratory experiments with ice-infiltrated powders (Cahn et al., 1992). Red dot-dashed curves show the predicted liquid saturation when the phase boundary is treated as locally hemispherical whenever it intersects a test point, labeled as throat total curve. Black dashed curves idealize the curvature-dominated liquid that remains after the formation of the first pore ice as residing in crevice regions where the phase boundary has two principal radii of curvature of opposite sign, labeled as crevice total curve. (a) Comparison between model predictions and calorimetry data for ice melting in mono-dispersed graphitized carbon black powder with average radius $r \approx 0.12\,\mu\text{m}$ and $\lambda_0 = 1.75\,\text{nm}$. The crevice total curve, although deviated from the measured data at higher liquid saturation, converges to the data points and the throat total curve after the saturation falls below 10%. A similar pattern occurs in (b) with calorimetry data for ice melting in mono-dispersed polystyrene powder with average radius $r \approx 2.5\,\mu\text{m}$ and the same $\lambda_0 = 1.75\,\text{nm}$. The asymptomatic curves for simple cubic (blue) and face-centered cubic (cyan) packings are shown for comparison. It must be noted that these curves are calculated with different fit radii. In (a), the fit radius is $0.1\,\mu\text{m}$, and in (b), as Dash et al. (2006) noted, the fit radius is $1.5\,\mu\text{m}$.

Figure 5 compares our model results to laboratory data (Cahn et al., 1992) for ice—water equilibrium within powders composed of (a) graphitized carbon black (taken from Maruyama et al., 1992) and (b) polystyrene. These powders consist of nearly mono-dispersed randomly packed particles with radii of 0.12 µm and 2.5 µm respectively. The detailed nature of the intermolecular forces that control changes in the thickness of premelted films is the least well-constrained part of our calculation. In our models, we keep $b = 3$ and $P_0 = 1.1\,\mathrm{MPa}$, with $\lambda_0 = 1.75\,\mathrm{nm}$ for both graphitized carbon black (Figure 5a) and polystyrene (Figure 5b). Both plots share similar features, notably that at higher liquid saturations, the throat total curve better describes the data points, whereas below 10% liquid saturation, the crevice total and throat total curves converge because wetting effects are responsible for most of the residual liquid under such conditions. For comparison, the curves for simple-cubic and face-centered cubic packings are also calculated following the asymptotic formulae in Cahn et al. (1992), shown as blue and cyan curves. We emphasize that the reported particle sizes for these powders were used to generate the synthetic particle packs leading to the model predictions shown in Figure 5, whereas the Cahn et al. (1992) theoretical curves treated the particle radius as a fitting parameter (Dash et al., 2006).

4.3 Comparison with liquid retention in the vadose zone

Water adsorbs to sediment particles in gas-infiltrated media, perhaps most notably within the vadose zone. This important effect is a consequence of the same mechanisms that cause undercooling in ice—liquid systems. In natural soil, comprised of particles with a range of different surface properties, the dominant intermolecular forces may cause wetting effects to be stronger or weaker (or both) than in laboratory prepared mono-dispersed powders. Moreover, the presence of non-spherical particles undoubtedly has a dramatic effect on the ability of our sphere-packing algorithm to replicate the pore geometry accurately, thereby affecting our ability to predict disturbances to the chemical potential caused by the pore geometry. The most obvious complication, however, is that natural soils are composed of particularly broad ranges of particle sizes. The Millville silt-loam examined by Or and Hanks (1992) serves as an illustrative example, comprised of 33% sand by mass, 49% silt, and 18% clay, with a reported specific surface area of $73\,\mathrm{m}^2/\mathrm{g}$. Further details of the particle size distribution were not reported, so we do not have sufficient information to construct a realistic synthetic packing. Based on standard parti-

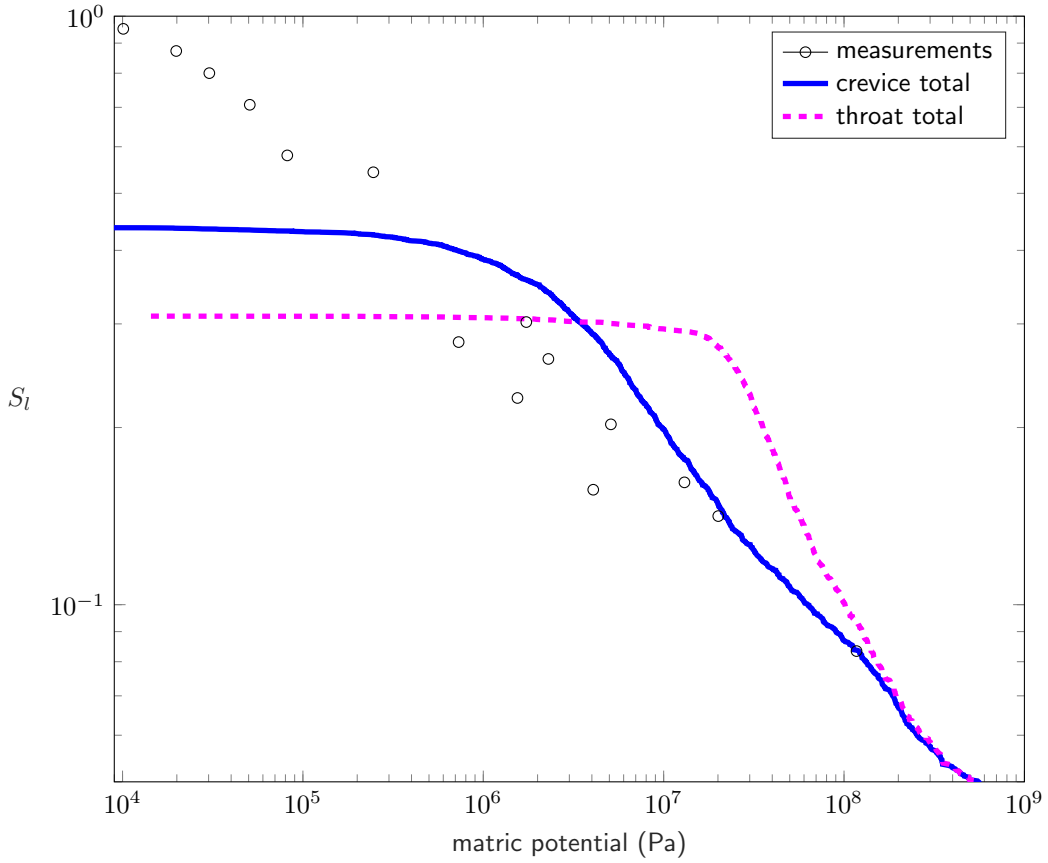

Figure 6. Model predicted matric potential curve (solid blue and dashed magenta) versus matric potential data from Or and Hanks (1992) (open circles). At low liquid saturations (below 10%) wetting effects dominate so the pore total curve and the crevice total curve are nearly identical for the assigned characteristic film thickness $\lambda_0 = 1.4\,\text{nm}$. At intermediate saturations ($10\% \leq S_l \leq 30\%$) the two curves diverge due to their differing treatments of the interface geometry near particle contacts; in this regime, curvature effects are well-represented by the crevice total curve, which closely approximates the observed saturation behavior. Our mono-dispersed particle simplification overestimates curvatures at higher saturations.

cle size classifications, however, the minimum diameter of sand particles can be 32 to 128 times the diameter of the largest clay particles, and if the particles are assigned a silica density of $2650\,\mathrm{kg/m^3}$, with the given mass fractions of the silt loam, the number of clay particles clearly dominates the total particle count.

At large matric potentials (and low liquid saturations), wetting is expected to give rise to most of the residual liquid volume. Treating λ_0 as a simple fitting parameter should enable us to match the saturation behavior in the film-dominated regime; a more stringent test of the limitations of our algorithm concerns the degree to which it can also capture the behavior at intermediate saturations where curvature effects have more control on the residual liquid volume than wetting. Accordingly, we construct a packing of particles with uniform radius $r_m \approx 0.0155\,\mu\mathrm{m}$ that is chosen to match the measured specific surface area. Figure 6 compares our model predictions for the matric potential of Millville silt loam (with $\lambda_0 = 1.4\,\mathrm{nm}$) against experimental results (Or & Hanks, 1992; Or & Tuller, 1999; Tuller & Or, 2005). At lower matric potentials the liquid saturation plateaus as a consequence of our neglect of the contributions from sand and silt, which causes our algorithm to underestimate the largest pore sizes, thereby lowering the liquid saturation required to reach a given curvature. Reasonable agreement between the experimental measurements and our crevice total curve is achieved below a saturation level of approximately 30%. The difference between the crevice total and throat total curves in the intermediate saturation regime between approximately 10% and 30% is due solely to differences in the treatment of the vapor—liquid interface geometry and its influence on the surface energy. With better constraints in the grain size distribution, the throat total curve should be able to describe the matric potential at higher saturations. This test demonstrates the ability of our algorithm to capture observed saturation changes outside of the realm where wetting effects dominate. Considering the simplicity of our treatment, with no attempt to account for the complexities of natural soil structure, the correspondence shown in Figure 6 between modeled and observed soil moisture in the intermediate saturation regime that we targeted for this illustration is encouraging.

4.4 Comparison with liquid saturation inferred from mercury porosimetry

Mercury porosimetry is commonly used to infer pore size distributions from the applied pressure needed to enable non-wetting mercury to overcome the surface-energy bar-

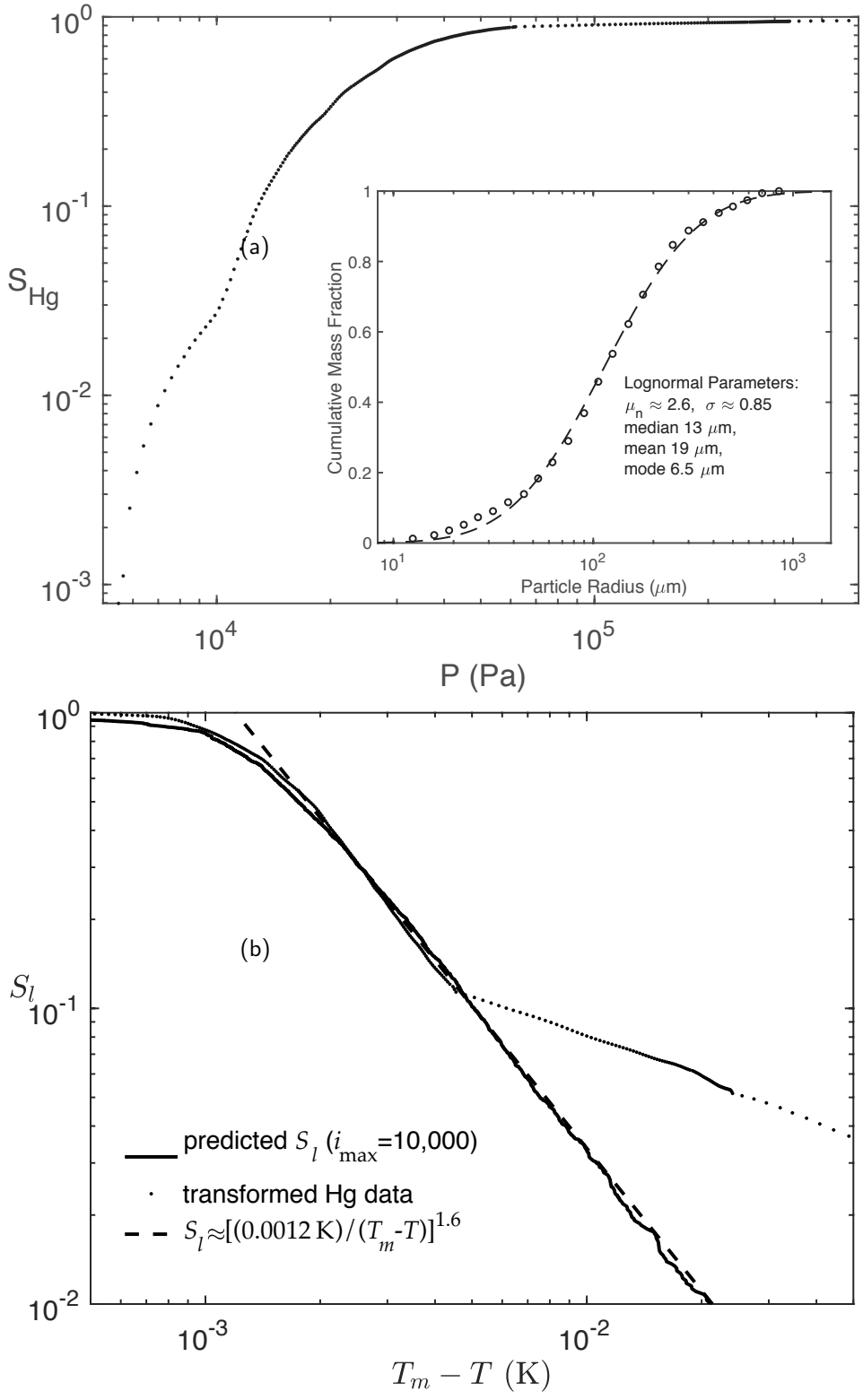

Figure 7. Saturation behavior in Beacon Valley sediments. (a) Measured mercury saturation as a function of pressure (Sizemore & Mellon, 2008). Inset shows the measured particle size distribution (circles) with the dashed curve representing the best-fit log-normal distribution. The labeled parameter values that define this log-normal distribution (see text) are expressed on the basis of particle count rather than particle mass. (b) Comparison between predicted liquid saturation based on $i_{\max} = 10,000$ sample points (solid line) and transformed porosimetry data (points). Also shown with a dashed line is a power law that approximates the data faithfully in the range $0.1 \leq S_l \leq 0.7$.

rier and enter dry pores. Figure 7a shows the reported Hg saturation level as a function of pressure in a soil from Beacon Valley, Antarctica, which is characterized by the measured cumulative particle size distribution shown in the inset (Sizemore & Mellon, 2008). Residual air persists in the pore space as a result of both surface energy and wetting effects. Recognizing, however, that the dynamics of frost processes are most active at high liquid saturations in which residual liquid volumes can be attributed primarily to surface energy rather than wetting effects, in this limit the mercury pressure at any particular saturation level can be converted to an approximate corresponding undercooling as follows. First, we recognize that the data for $P(S_{\rm Hg})$ should be proportional to $\gamma_{\rm Hg}\cos(\theta)$, where the surface tension of the air—Hg interface is $\gamma_{\rm Hg} \approx 0.46\,{\rm J/m^2}$ and $\theta \approx 140^\circ$ is the contact angle of Hg—air—particle surfaces. At an equivalent ice saturation $S_{\rm ice} = 1 - S_l$ we expect $P_i(S_{\rm ice} \approx S_{\rm Hg})$ should be proportional to the ice—liquid surface energy γ (assuming that liquid water wets matrix particles completely in preference to ice, so the contact angle is 0°). This suggests a simple conversion wherein

$$\frac{P_i(S_{\rm ice})}{P(S_{\rm Hg})} \approx -\frac{\gamma}{\gamma_{\rm Hg}\cos(\theta)} \approx 0.082. \tag{9}$$

Inserting this expression into eq. (4) leads to the following approximation for the undercooling that corresponds to a given mercury pressure

$$\Delta T = -\frac{T_m}{\rho_i L}\frac{\gamma}{\gamma_{\rm Hg}\cos(\theta)} P(S_{\rm ice} \approx S_{\rm Hg}). \tag{10}$$

Figure 7b shows the undercooling obtained from eq. (10) as a function of the wetting liquid water saturation that is expected to coexist with non-wetting ice, as inferred from the mercury porosimetry measurements. The solid black line gives model saturation predictions based on sampling at $i_{\rm max} = 10,000$ discrete points. The agreement between these two independent approximations is extremely good for $S_l > 10\%$. Moreover, the close correspondence with the dashed line suggests that a simple power law also fits the behavior well over this upper range of liquid saturation levels. By contrast, once the mercury pressure (and the equivalent undercooling from eq. (10)) is high enough for S_l to drop below about 10% (i.e., once $S_{\rm Hg}$ exceeds 90%) the porosimetry points in Figure 7b begin to deviate significantly from the model predictions. We note that the model curve does depart from the power-law trend once the undercooling is large enough that $S_l < 1\%$ and the liquid volume held in wetting films becomes an appreciable fraction of the total. This suggests a potential strategy for better matching the mercury-based inferences at low S_l by increasing the film thickness parameter λ_0 from its nominal value

of 3.5 nm. However, as there is no basis for expecting the wetting behavior in an ice—liquid—particle system to be well represented by the wetting behavior in a Hg–air—particle system, we see little merit in pursuing such a fitting exercise.

The synthetic particle pack that we sampled in order to generate the saturation predictions shown in Figure 7b was based on the measured particle size distribution for this Beacon Valley soil (Sizemore & Mellon, 2008). As shown in the inset to Figure 7a the particle size distribution is approximately log-normal, so that the cumulative distribution of particle radii can be expressed as

$$C(r) = \frac{1}{2}\left[1 + \mathrm{erf}\left(\frac{\ln r - \mu_n}{\sqrt{2}\sigma}\right)\right], \tag{11}$$

where the median particle radius is $r_m = \exp(\mu_n)$ and σ is the standard deviation of $\ln r$. It is common practice to report particle size distributions on a mass or volume fraction basis whereas our packing routine is more naturally compatible with number-based distribution functions. Fortunately, a simple conversion enables the number-based parameter μ_n to be obtained from its volume-based counterpart μ_v as $\mu_n = \mu_v - 3\sigma^2$. At values of S_l large enough for wetting films to represent a negligible fraction of the residual liquid volume (i.e., $S_l > 10\%$) the close correspondence between the model predicted saturation in the log-normally distributed synthetic particle pack and the transformed mercury data is obtained with no adjustable parameters.

4.5 Predicted SFCs for log-normally distributed particle packs

Having demonstrated reasonable agreement between our model predictions and several independent assessments of saturation changes, we next illustrate the capabilities of our algorithm by predicting SFC behavior for the family of porous media that can be approximated using close-packed, spherical particles with log-normally distributed radii. Figure 8a shows the cumulative distribution of particles described by eq. (11) as a function of their radii r normalized by the median radius $r_m = \exp(\mu_n)$. Mono-dispersed packings are represented by the case with $\sigma = 0$ so that the median, mean, and mode of the particle radii all coincide at $r/r_m = 1$. The parameter σ is linearly related to the inclusive graphic standard deviation σ_I (Folk, 1966) commonly defined in sedimentology and soil science as $\sigma_I = \sigma/\ln 2$; at larger $\sigma \sim \mathcal{O}(1)$, the particles are categorized as poorly sorted. We used these distributions in our sphere-packing algorithm to generate synthetic porous media and examine their predicted SFCs, which are shown in Fig-

ure 8b. To reveal the controlling effects of curvature alone, we examine the limit in which $\lambda_0 = 0$ so that the curvature in eq. (2) can be scaled with the median particle radius to obtain

$$T_m - T \approx \frac{T_m \gamma}{\rho_i L} \mathcal{K} \approx \frac{0.026\,\mathrm{K\,\mu m}}{r_m} \mathcal{K} r_m, \tag{12}$$

which sets the scale for the saturation plot in Figure 8b. For example, a scaled curvature of $\mathcal{K} r_m = 1$ corresponds with $(T_m - T)\big|_{\mathcal{K} r_m = 1} \approx 0.026\,\mathrm{K}$ for $r_m = 1\,\mu\mathrm{m}$, whereas $(T_m - T)\big|_{\mathcal{K} r_m = 1} \approx 0.0026\,\mathrm{K}$ for $r_m = 10\,\mu\mathrm{m}$. The saturation predictions clearly indicate that the onset of freezing takes place at smaller scaled curvatures, or equivalently smaller undercoolings, as σ is increased to characterize correspondingly broader distributions of particle sizes. This result is suggestive of the influence of anomalously large pores in which ice formation can take place at much lower undercoolings than in pores bounded entirely by median-sized particles. It seems plausible that a different packing algorithm designed to ensure that small particles occupy the spaces between larger particles (e.g., simulating particle redistribution resulting form winnowing, shaking, or other disturbances), might be employed to produce smaller characteristic pore sizes (and lower porosities); we leave further exploration of this possibility to future work. Also of note are the consistent slopes to the saturation changes with scaled curvature on this log-log plot, suggesting that the saturation behavior is well approximated in each of these curvature-dominated cases by a power-law dependence on undercooling with an exponent that falls within a fairly narrow range spanned approximately by 1.6 and 2.0. The exponent appears to be determined primarily by the geometry of the crevices in between spherical particles.

Figure 9a explores the influence of wetting interactions on the saturation behavior, for the different values of λ_0 given in the legend, with $r_m = 1\,\mu\mathrm{m}$ in each case (we keep $b = 3$, $P_0 = 1.1\,\mathrm{MPa}$). As the saturation level decreases, an increasing proportion of the residual liquid volume is held in wetting films, and higher values of λ_0 cause the transition away from surface-energy dominated liquid volumes to film-dominated liquid volumes to occur at higher values of S_l. Figure 9b displays the changes in the relative importance of wetting effects as r_m is increased while $\lambda_0 = 3.5\,\mathrm{nm}$ is held constant. Because of reductions in the surface area to volume ratios of representative pores, as r_m is increased the transition from surface-energy dominated liquid volumes to film-dominated liquid volumes takes place at lower S_l. We note that SFCs are often approximated with a simple power law dependence of saturation on the undercooling, as illus-

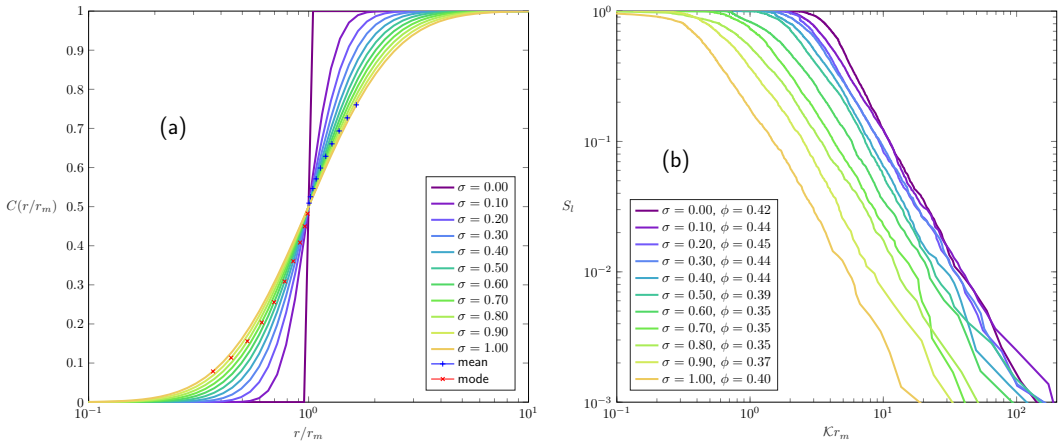

Figure 8. SFCs for log-normally sized particles. (a) Cumulative distribution plotted as a function of radius scaled by the median $r_m = \exp(\mu_n)$ so that $C(1) = 0.5$ in all cases. Different curves are used to represent different values of σ, which is the standard deviation of $\ln r$. Also plotted are the mean and mode radii for each distribution. (b) Predicted saturation curves plotted as a function of the scaled curvature $\mathcal{K}r_m$, with calculated porosities ϕ shown in the legend.

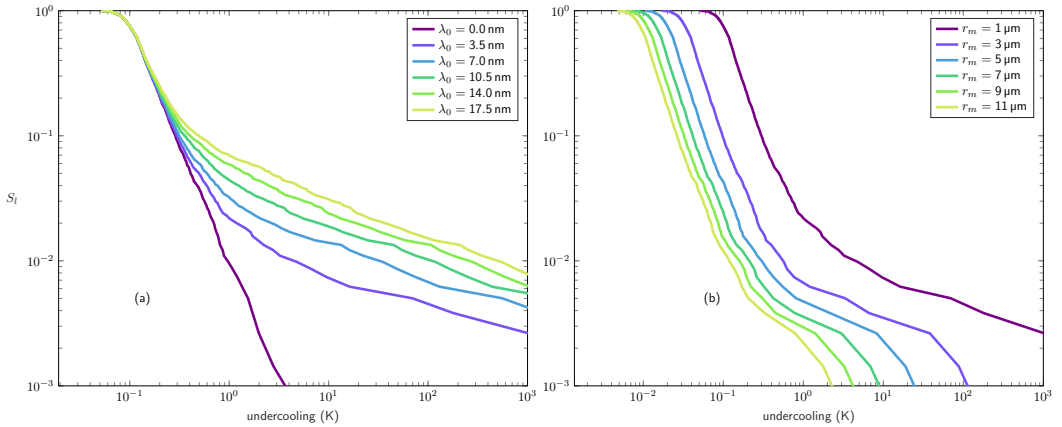

Figure 9. Effects of wetting parameters λ_0 and r_m on the SFCs for mono-dispersed soil particles. In (a), the median particle radius is kept at 1 µm, while λ_0 increases from zero to 17.5 nm. As more water is retained in films, their role becomes significant at higher liquid saturations. In (b), λ_0 is kept at 3.5 nm, while r_m is increased from 1 to 11 µm. With larger particle sizes, the overall pore volume increases, and the liquid in films is less important in determining the SFCs.

trated by the dashed line in Figure 7. Published power-law exponents for SFCs (e.g., Orlando B. Andersland, 2003) are often smaller than the 1.6–2.0 values that characterize the simulation results shown in Figure 8b. Figure 9 suggests that experimental data collected across the transition from surface-energy dominated to film-dominated liquid volumes might provide an explanation for inferred modest power-law slopes.

The colligative effects of dissolved solutes may also alter the slopes of SFCs. As residual liquid volumes are diminished upon cooling, the elevated solutal concentration significantly increases the additional undercooling required for freezing to occur. In Figure 10a and Figure 10b, we calculate the SFCs for a mono-dispersed porous medium with $r_m = 1\,\mu\text{m}$ and $\lambda_0 = 0$, saturated with water doped by two common chloride salts and two perchlorate salts at different initial concentrations using the method outlined in Appendix B. Even with low m_s ($< 1\,\text{wt}\%$), high solutal concentration at relatively low liquid contents (i.e., $S_l < 10\%$) still results in much gentler slopes (i.e., power-law exponents) than those predicted for pure water. The undercooling of liquid water caused by perchlorate salts, for example in the Martian regolith, leads to the SFCs produced in Figure 10c to Figure 10f, with $\lambda_0 = 9\,\text{nm}$, and $r_m = 1\,\mu\text{m}$ and $r_m = 50\,\mu\text{m}$. In agreement with previous work (e.g., Hansen-Goos & Wettlaufer, 2010), these calculations also demonstrate a tendency towards a power-law slope of -1 at high solute concentrations and smaller particle sizes. We note that detected perchlorate concentrations at the Phoenix lander site were comparable to 1 wt% (e.g., Hecht et al., 2009; Toner et al., 2014), for which the power-law slopes displayed in Figure 10c to Figure 10f are $\beta \approx 1.1$.

5 Discussion

5.1 Film behavior

The power-law description of film thickness defined by eq. (3) represents a useful approximation that is supported both by theoretical considerations and empirical evidence in particular systems (Dash et al., 2006). For example, non-retarded van der Waals interactions yield this functional form for the relationship between P_T and d with an exponent of $b = 3$, in agreement with optical observations by Sadtchenko and Ewing (2002) and wire regelation experiments by Gilpin (1980). The limiting case of short-range electrostatic interactions that satisfy the Langmuir approximation is expected to produce $b = 1.5$, consistent with inferences based on ice lens experiments by Saruya et al. (2014).

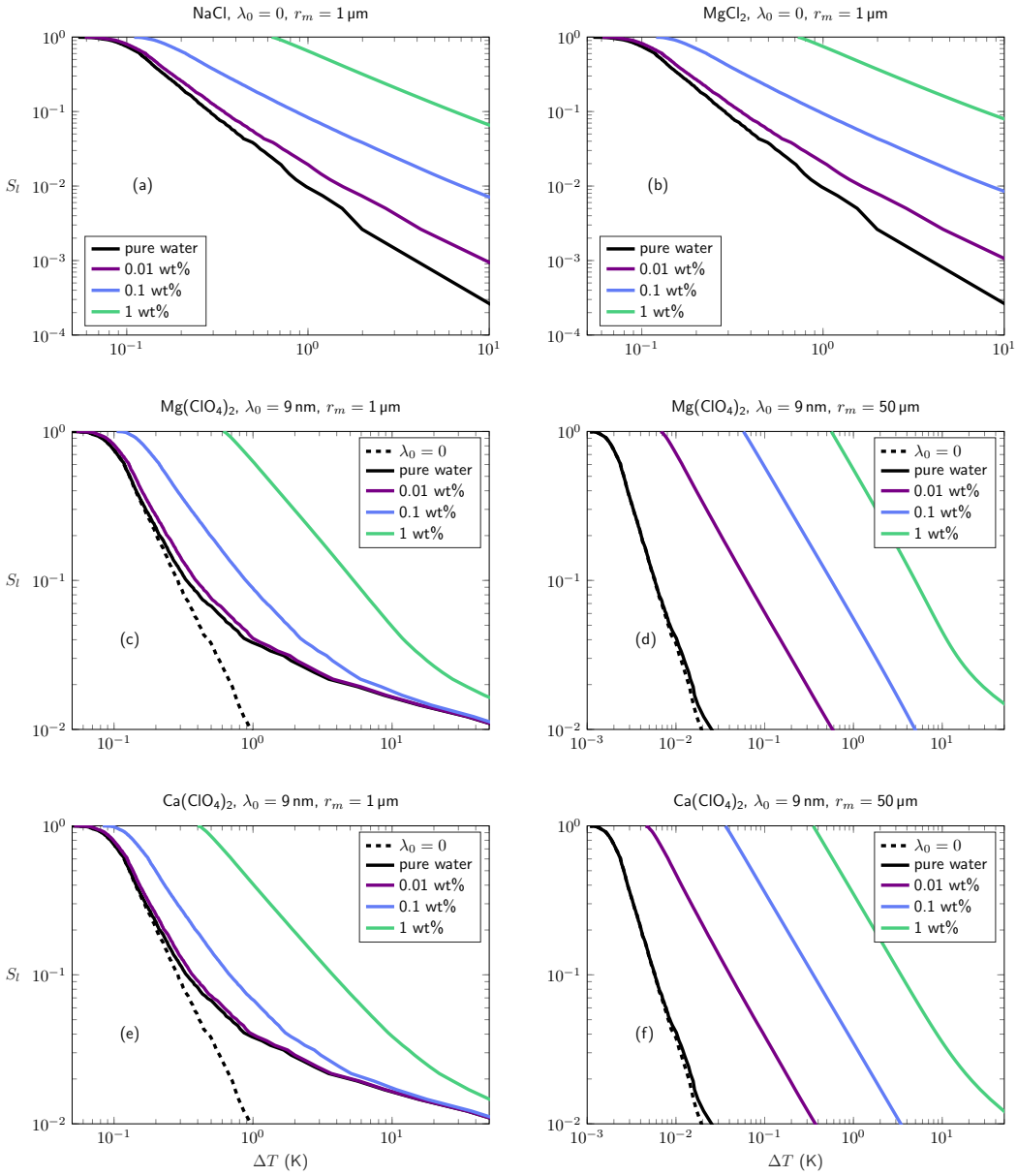

Figure 10. Comparison of SFCs of salt-doped liquid with the SFC of pure water in monodispersed powders. Wetting effects are ignored and $r_m = 1\,\mu m$ in (a) and (b), where the solutes are NaCl and $MgCl_2$, respectively. For lower initial concentration of 0.01 wt% (purple), the SFCs only slightly deviate from those of pure water (black), but with higher concentrations, e.g., 0.1 wt% (blue) and 1 wt% (green), the undercoolings caused by solutes are significantly higher, and the power-law slopes of the SFCs are much smaller than the value of ~ 2 that characterizes the pure water case. The effects of wetting are included with $\lambda_0 = 9\,nm$ for water doped by magnesium perchlorate in (c) with $r_m = 1\,\mu m$ and (d) with $r_m = 50\,\mu m$, and by calcium perchlorate in (e) with $r_m = 1\,\mu m$ and (f) with $r_m = 50\,\mu m$. In the perchlorate plots, black dashed lines indicate the pure water cases without wetting, demonstrating that their effects are negligible at elevated S_l and larger r_m.

However, more detailed analysis of the relationship between P_T and d suggest that a single power law is likely to describe film thickness variations over only a restricted range. Moreover, screened Coulomb interactions are anticipated to yield a logarithmic dependence of d on P_T, and transitions that include much more exotic behavior are anticipated, particularly as solute content and surface charge vary (see e.g., Hansen-Goos & Wettlaufer, 2010; Israelachvili, 2011). Our focus on the high liquid-saturation range limits the influence of films on our predictions, but these complications can exert a strong influence on the liquid saturation at larger undercoolings where films are volumetrically dominant. Indeed, the results displayed in Figure 9 provide guidance for the saturation range over which film behavior has a negligible influence on the total liquid content. This is shown by the convergence of predicted saturation behavior with different λ_0 when $S_l > 0.1$ and $r_m = 1\,\mu\text{m}$ (Figure 9a), and the apparent extension of the curvature dominated regime to still lower values of S_l as the particle radius is increased (Figure 9b).

5.2 Limitations of soil modeling using spherical particles

We have demonstrated that reasonably accurate SFC predictions can be generated by treating sediments as assemblages of randomly packed spherical particles. This approach requires first building a synthetic model soil with an appropriate particle size distribution. However, as in the case of the Millville silt-loam, natural soils can have very broad ranges of particle sizes. For that particular example, although the mass fractions of sand and silt are higher than that of clay, the number count is dominated by the much smaller clay particles, which control the specific surface area. In fact, the number density of clay particles is so high that in a pack of $\sim 10^5$ particles there are essentially no silt or sand particles. This observation motivated our strategy of approximating portions of the SFC by considering a porous medium comprised of only the clay-sized fraction. Whereas the plate-like geometry of clay particles is quite different from the spherical geometry of the particles in our synthetic soil pack, the reasonable agreement between data and model calculations illustrated in Figure 6 gives support for the strategy of choosing the spherical particle size so that the specific surface area of the synthetic soil matches its measured counterpart. This approach was taken to ensure that the liquid fraction in the film-dominated regime could be well approximated, but Figure 6 reveals that the favorable comparison with measurements extends up to liquid saturations that are high enough for surface-energy effects to control the liquid saturation. Nevertheless, it is im-

portant to recognize that neglect of the larger particle size fraction causes the pore size distribution of our synthetic soil to differ from the actual pore size distribution, which is expected to include a population of pores that are larger than any we account for; this leads to inaccurate predictions as the liquid saturation is raised higher still and approaches unity.

5.3 Potential contributions of grain-boundary melting

In the calculations presented here, all residual liquid beyond that due to solutes is attributed solely to the effects of surface energy and interfacial premelting against the surfaces of matrix particles. Additional contributions from premelting along grain boundaries (e.g., Benatov & Wettlaufer, 2004; Thomson et al., 2013) and in grain-boundary grooves (e.g., Hardy, 1977) may be significant, particularly for smaller ice crystals. Following the strategy of Cahn et al. (1992), these effects might be approximated for the case where each pore contains a single ice crystal that meets with its neighbors at pore throats in association with two-grain boundaries and grain boundary grooves. Future efforts that build upon this idea would benefit from empirical data to validate the approach and also explore potential effects of crystal size evolution (i.e., ripening).

5.4 Analogue to gas hydrate in marine sediments

Gas hydrates are ice-like compounds where gas molecules (mainly CH_4) occupy cages (clathrates) formed by water molecules. Hydrate deposits occur widely on continental margins and in permafrost. Similar to ice in soils, the equilibrium of gas hydrate with aqueous solutions containing dissolved methane is shifted within porous sediments. In finer sediments with smaller pores, the curved hydrate—water interface elevates the chemical potential of hydrates, and consequently equilibrium coexistence requires either cooler temperatures for a particular concentration of dissolved methane or higher dissolved methane concentration at any particular temperature. At a given pressure, the undercooling follows a form similar to eq. (2), with

$$\Delta T = T_m - T = \frac{T_m}{\rho_h L} \left(\gamma_{hw} \mathcal{K} + P_T \right), \tag{13}$$

where the hydrate density $\rho_h \approx 929\,\mathrm{kg/m^3}$, $L \approx 435\,\mathrm{kJ/kg}$, γ_{hw} is expected to be comparable to the surface energy of the liquid—ice interface, and T_m is the bulk dissociation temperature. The elevated chemical potential of dissolved methane at a concentra-

tion c in excess of the bulk equilibrium concentration c_m is

$$\Delta\mu = RT_m \ln\left(\frac{c}{c_m}\right) = V_H\left(\gamma_{hw}\mathcal{K} + P_T\right) \tag{14}$$

where R is the gas constant and V_H is the volume of methane hydrate per mole of methane. By introducing the dissociation enthalpy change $\Delta H \approx 54\,\mathrm{kJ/mol}$, which is related to latent heat through $L = \Delta H/(\rho_h V_H)$, the concentration of dissolved methane in equilibrium with pore-bound crystalline hydrate can be written as

$$c = c_m \exp\left[\frac{\Delta H}{\rho_h L R T_m}\left(\gamma_{hw}\mathcal{K} + P_T\right)\right] = c_m \exp\frac{\Delta T}{\alpha} \tag{15}$$

where the temperature scale α is defined as (e.g., Davie et al., 2004)

$$\alpha = \frac{RT_m^2}{\Delta H}. \tag{16}$$

It is straightforward to use our approach to evaluate the geometrical constraints on $\mathcal{K}$ and P_T and quantitatively predict the pore-scale controls on gas hydrate equilibria that are needed as input to models for the heterogeneous distribution of hydrates in marine sediments (e.g., A. W. Rempel, 2011; VanderBeek & Rempel, 2018).

5.5 Implications for extraterrestrial ice-covered environments

Many extraterrestrial satellites and planets, including Mars, host ice (or hydrate) in near-surface soils. Despite being subject to low ambient temperatures, high curvatures and high salinities facilitate the equilibrium presence of small amounts of residual liquid moisture in association with this ice. The implications for many of the same dynamic interactions that drive phenomena such as frost heave in terrestrial soils and provide habitat for microbial communities have yet to be fully explored. The numerical procedures (Chen & Rempel, 2019a, 2019b) used to generate the SFCs shown here can be adapted easily to facilitate further work in this vein.

6 Conclusion

Our calculations and validation tests demonstrate that the temperature dependence of liquid saturation in porous media can be approximated reasonably well by analyzing the local geometrical constraints on phase equilibrium at a sequence of randomly chosen sample points in a synthetic porous medium comprised of an appropriate distribution of spheres. Over a broad range of liquid saturations, model predictions fit well with

experimental data and require no adjustable parameters at sufficiently high saturations (i.e., $S_l > 10\%$), so that the effects of surface energy and curvature dominate in the absence of solutes. Within this high-saturation regime, the liquid content in close-packed porous media constructed with lognormally distributed particles is well approximated by a simple power-law with a threshold temperature for ice infiltration that is smaller in less well-sorted sediments and an exponent that is close to 2 in the mono-dispersed limit. At lower saturations, the effects of wetting produce more gradual changes in saturation level with temperature. When the colligative effects of solutes dominate the liquid content, a power law exponent approaching unity best approximates the saturation behavior. Our approach provides a method to quantitatively determine pore scale effects on the liquid—ice phase transition, and shed lights on similar two-phase liquid—solid or liquid—vapor systems on Earth and beyond.

Acknowledgments

The data used are listed in the references and tables. JC was supported by funding from the National Natural Science Foundation of China (Grant No. 41804085), and also from the Key Laboratory of Gas Hydrate, Guangzhou Institute of Energy Conversion, Chinese Academy of Sciences (Grant No. Y807KF1001). SM was supported by Chinese Academy of Sciences (No. QYZDY-SSW-DQC029) and the National Natural Science Foundation of China (No. 41674097). AWR and JTI received funding from the U.S. Department of Energy (Grant No. DE-FE0013565).

References

Altheide, T., Chevrier, V., Nicholson, C., & Denson, J. (2009, May). Experimental investigation of the stability and evaporation of sulfate and chloride brines on mars. *Earth Planet. Sci. Lett.*, *282*(1-4), 69–78. doi: 10.1016/j.epsl.2009.03.002

Bakker, R. J. (2012, February). Package FLUIDS. part 4: thermodynamic modelling and purely empirical equations for h2o-NaCl-KCl solutions. *Mineral. Petrol.*, *105*(1-2), 1–29. doi: 10.1007/s00710-012-0192-z

Benatov, L., & Wettlaufer, J. S. (2004, December). Abrupt grain boundary melting in ice. *Phys Rev E: Stat , Nonlinear, Soft Matter Phys*, *70*(6). doi: 10.1103/physreve.70.061606

Cahn, J., Dash, J., & Fu, H. (1992, September). Theory of ice premelting in monosized powders. *J. Cryst. Growth*, *123*(1-2), 101–108. doi: 10.1016/0022-0248(92)90014-a

Chen, J., & Rempel, A. (2019a). *Ice in granular media.* https://gitlab.com/jzchenjz/ice-in-granular-media.

Chen, J., & Rempel, A. (2019b). *Packing of spherical particles.* https://gitlab.com/jzchenjz/packing-of-spherical-particles.

Coxeter, H. S. M. (1968, January). The problem of apollonius. *Am. Math. Mon.*, *75*(1), 5–15. doi: 10.2307/2315097

Dash, J. G., Rempel, A. W., & Wettlaufer, J. S. (2006, July). The physics of premelted ice and its geophysical consequences. *Rev. Mod. Phys.*, *78*(3), 695–741. doi: 10.1103/revmodphys.78.695

Davie, M., Zatsepina, O. Y., & Buffett, B. (2004, January). Methane solubility in marine hydrate environments. *Mar. Geol.*, *203*(1-2), 177–184. doi: 10.1016/s0025-3227(03)00331-1

Denoyel, R., & Pellenq, R. J. M. (2002, April). Simple phenomenological models for phase transitions in a confined geometry. 1: Melting and solidification in a cylindrical pore. *Langmuir*, *18*(7), 2710–2716. doi: 10.1021/la015607n

Depriester, D., & Kubler, R. (2019, February). Radical voronoï tessellation from random pack of polydisperse spheres: Prediction of the cells' size distribution. *Comput.-Aided Des.*, *107*, 37–49. doi: 10.1016/j.cad.2018.09.001

Fisher, R. A. (1926, July). On the capillary forces in an ideal soil; correction of formulae given by w. b. haines. *J. Agric. Sci.*, *16*(03), 492. doi: 10.1017/s0021859600007838

Folk, R. L. (1966, March). A review of grain-size parameters. *Sedimentology*, *6*(2), 73–93. doi: 10.1111/j.1365-3091.1966.tb01572.x

Gilpin, R. R. (1980, October). A model for the prediction of ice lensing and frost heave in soils. *Water Resour. Res.*, *16*(5), 918–930. doi: 10.1029/wr016i005p00918

Hallet, B., Walder, J. S., & Stubbs, C. W. (1991, October). Weathering by segregation ice growth in microcracks at sustained subzero temperatures: Verification from an experimental study using acoustic emissions. *Permafrost Periglacial Processes*, *2*(4), 283–300. doi: 10.1002/ppp.3430020404

Handwerger, A. L., Rempel, A. W., & Skarbek, R. M. (2017, July). Submarine landslides triggered by destabilization of high-saturation hydrate anomalies. *Geochem. Geophys. Geosyst.*, *18*(7), 2429–2445. doi: 10.1002/2016gc006706

Hansen-Goos, H., & Wettlaufer, J. S. (2010, March). Theory of ice premelting in porous media. *Phys. Rev. E: Stat., Nonlinear, Soft Matter Phys.*, *81*(3), 031604. doi: 10.1103/physreve.81.031604

Hardy, S. C. (1977, February). A grain boundary groove measurement of the surface tension between ice and water. *Philos. Mag.*, *35*(2), 471–484. doi: 10.1080/14786437708237066

Hecht, M. H., Kounaves, S. P., Quinn, R. C., West, S. J., Young, S. M. M., Ming, D. W., ... Smith, P. H. (2009, July). Detection of perchlorate and the soluble chemistry of martian soil at the phoenix lander site. *Science*, *325*(5936), 64–67. doi: 10.1126/science.1172466

Israelachvili, J. N. (2011). *Intermolecular and surface forces.* Academic Press.

Jang, J., & Santamarina, J. C. (2011, August). Recoverable gas from hydrate-bearing sediments: Pore network model simulation and macroscale analyses. *J. Geophys. Res.*, *116*(B8). doi: 10.1029/2010jb007841

Jodrey, W. S., & Tory, E. M. (1979, January). Simulation of random packing of spheres. *Simulation*, *32*(1), 1–12. doi: 10.1177/003754977903200102

Kim, Y. P., & Seinfeld, J. H. (1995, January). Atmospheric gas–aerosol equilibrium: III. thermodynamics of crustal elements ca^{2+}, k^{+}, and mg^{2+}. *Aerosol Sci. Technol.*, *22*(1), 93–110. doi: 10.1080/02786829408959730

King, M. B. (1969). *Phase equilibrium in mixtures.* Elsevier Science. Retrieved from `https://www.ebook.de/de/product/23258401/m_b_king_phase_equilibrium_in_mixtures.html`

Lipovsky, B. P., Meyer, C. R., Zoet, L. K., McCarthy, C., Hansen, D. D., Rempel, A. W., & Gimbert, F. (2019, June). Glacier sliding, seismicity and sediment entrainment. *Ann. Glaciol.*, *60*(79), 182–192. doi: 10.1017/aog.2019.24

López, R. (2013). *Constant mean curvature surfaces with boundary.* Springer-Verlag GmbH. Retrieved from `https://www.ebook.de/de/product/20827355/rafael_lopez_constant_mean_curvature_surfaces_with_boundary.html`

Maruyama, M., Bienfait, M., Dash, J., & Coddens, G. (1992, March). Interfacial melting of ice in graphite and talc powders. *J. Cryst. Growth*, *118*(1-2), 33–40.

694 doi: 10.1016/0022-0248(92)90046-l

695 Meyer, C. R., Downey, A. S., & Rempel, A. W. (2018, August). Freeze-on limits bed
696 strength beneath sliding glaciers. *Nat. Commun.*, *9*(1). doi: 10.1038/s41467
697 -018-05716-1

698 Or, D., & Hanks, R. J. (1992). Soil water and crop yield spatial variability induced
699 by irrigation nonuniformity. *Soil Sci. Soc. Am. J.*, *56*(1), 226. doi: 10.2136/
700 sssaj1992.03615995005600010035x

701 Or, D., & Tuller, M. (1999, October). Liquid retention and interfacial area in
702 variably saturated porous media: Upscaling from single-pore to sample-scale
703 model. *Water Resour. Res.*, *35*(12), 3591–3605. doi: 10.1029/1999wr900262

704 Orlando B. Andersland, A. S. C. E., Branko Ladanyi. (2003). *Frozen ground engi-*
705 *neering*. John Wiley & Sons Inc.

706 Pestova, O. N., Myund, L. A., Khripun, M. K., & Prigaro, A. V. (2005, March).
707 Polythermal study of the systems $M(ClO_4)_2$–H_2O (M^{2+} = Mg^{2+}, Ca^{2+}, Sr^{2+},
708 Ba^{2+}). *Russ. J. Appl. Chem.*, *78*(3), 409–413. doi: 10.1007/s11167-005-0306-z

709 Poling, B. E., Prausnitz, J. M., O'connell, J. P., et al. (2001). *The properties of*
710 *gases and liquids* (Vol. 5). Mcgraw-hill New York.

711 Rempel, A., & Rempel, A. (2016, August). Intrinsic evaporative cooling
712 by hygroscopic earth materials. *Geosciences*, *6*(3), 38. doi: 10.3390/
713 geosciences6030038

714 Rempel, A., & Worster, M. (1999, September). The interaction between a particle
715 and an advancing solidification front. *J. Cryst. Growth*, *205*(3), 427–440. doi:
716 10.1016/s0022-0248(99)00290-0

717 Rempel, A. W. (2010). Frost heave. *J. Glaciol.*, *56*(200), 1122–1128. doi: 10.3189/
718 002214311796406149

719 Rempel, A. W. (2011, October). A model for the diffusive growth of hydrate satu-
720 ration anomalies in layered sediments. *J. Geophys. Res. Solid Earth*, *116*(B10).
721 doi: 10.1029/2011jb008484

722 Rempel, A. W. (2012, April). Hydromechanical processes in freezing soils. *Vadose*
723 *Zone J.*, *11*(4), 0. doi: 10.2136/vzj2012.0045

724 Rempel, A. W., Marshall, J. A., & Roering, J. J. (2016, November). Modeling rela-
725 tive frost weathering rates at geomorphic scales. *Earth Planet. Sci. Lett.*, *453*,
726 87–95. doi: 10.1016/j.epsl.2016.08.019

Rempel, A. W., & Rempel, A. R. (2019, July). Frost resilience of stabilized earth building materials. *Geosciences*, *9*(8), 328. doi: 10.3390/geosciences9080328

Sadtchenko, V., & Ewing, G. E. (2002, March). Interfacial melting of thin ice films: An infrared study. *J. Chem. Phys.*, *116*(11), 4686–4697. doi: 10.1063/1.1449947

Saruya, T., Kurita, K., & Rempel, A. W. (2014, June). Indirect measurement of interfacial melting from macroscopic ice observations. *Phys. Rev. E: Stat., Nonlinear, Soft Matter Phys.*, *89*(6), 060401. doi: 10.1103/physreve.89.060401

Scherer, G. W. (1999, August). Crystallization in pores. *Cem. Concr. Res.*, *29*(8), 1347–1358. doi: 10.1016/s0008-8846(99)00002-2

Shi, Y., & Zhang, Y. (2008, May). Simulation of random packing of spherical particles with different size distributions. *Appl. Phys. A*, *92*(3), 621–626. doi: 10.1007/s00339-008-4547-6

Sizemore, H. G., & Mellon, M. T. (2008, October). Laboratory characterization of the structural properties controlling dynamical gas transport in mars-analog soils. *Icarus*, *197*(2), 606–620. doi: 10.1016/j.icarus.2008.05.013

Sizemore, H. G., Zent, A. P., & Rempel, A. W. (2015, May). Initiation and growth of martian ice lenses. *Icarus*, *251*, 191–210. doi: 10.1016/j.icarus.2014.04.013

Spivey, J., McCain, W., & North, R. (2004, July). Estimating density, formation volume factor, compressibility, methane solubility, and viscosity for oilfield brines at temperatures from 0 to 275 °c, pressures to 200 MPa, and salinities to 5.7 mole/kg. *J. Can. Pet. Technol.*, *43*(07). doi: 10.2118/04-07-05

Tang, I. N. (1997, January). Thermodynamic and optical properties of mixed-salt aerosols of atmospheric importance. *J. Geophys. Res. Atmos.*, *102*(D2), 1883–1893. doi: 10.1029/96jd03085

Thomson, E. S., Hansen-Goos, H., Wettlaufer, J. S., & Wilen, L. A. (2013, March). Grain boundary melting in ice. *J. Chem. Phys.*, *138*(12), 124707. doi: 10.1063/1.4797468

Toner, J., Catling, D., & Light, B. (2014, July). Soluble salts at the phoenix lander site, mars: A reanalysis of the wet chemistry laboratory data. *Geochim. Cosmochim. Acta*, *136*, 142–168. doi: 10.1016/j.gca.2014.03.030

Tuller, M., & Or, D. (2005, September). Water films and scaling of soil characteristic curves at low water contents. *Water Resour. Res.*, *41*(9). doi: 10.1029/

2005wr004142

VanderBeek, B. P., & Rempel, A. W. (2018, July). On the importance of advective versus diffusive transport in controlling the distribution of methane hydrate in heterogeneous marine sediments. *J. Geophys. Res. Solid Earth*, *123*(7), 5394–5411. doi: 10.1029/2017jb015298

Appendix A Monte Carlo method

A1 Sampling procedure

We select a large number of random test points within the test plane, and the fraction of test points that are not located in the pore space are used to estimate the solid fraction and its complement, the porosity. For each test point that lands within the pore space, we use the geometrical constraints imposed by the nearest particles to determine the magnitude of the equilibrium perturbation needed for ice to first encompass that point. This involves a series of calculations corresponding with the different scenarios described briefly below; at each test point the scenario requiring the smallest perturbation from bulk equilibrium is adopted as the best estimate for the conditions under which the wetting liquid is first excluded from that location. After the data are compiled, the residual liquid saturation is evaluated as the ratio of the number of test points that remain within the wetting phase at a particular perturbation relative to the total number of test points contained within the pore space.

A2 Largest inscribed spherical pore ice

The largest inscribed sphere either touches the four closest particles and has the test point inside, or touches the three closest particles and the test point at the same time. We find the largest inscribed pore ice by first inserting a spherical phase boundary into the pore with the test point as its center and the radius set by the distance to the nearest particle. The sphere is then grown by randomly moving its center point a small increment and changing its radius to match the new distance to the nearest particle. If the pore geometry and test point location do not permit a particular move without a decrease in pore radius, the move is rejected and an alternative perturbation is made instead. Iterations are halted after a set number of attempts is exceeded and incremental changes in the radius r_p fall below a threshold. As a final step, we identify the four closest par-

790 ticles to the sphere and solve for the small adjustment in position and radius necessary
791 to ensure tangency. We recognize this as a special case of the problem solved by the ge-
792 ometer and mystic, Apollonius, during the 3rd century BC (Coxeter, 1968). We view the
793 intuitive simplicity of our algorithm as advantageous, but note that further performance
794 improvements might be made by implementing more sophisticated methods, such as the
795 Voronoi diagram (e.g., Depriester & Kubler, 2019).

796 A3 Toroidal approximation of crevice ice

797 In crevice ice scenario, we envision the ice boundary forming a surface of revolu-
798 tion around the particle contact so that the first principal radius is the radius of the Apol-
799 lonius circle that intersects a given test point and the two adjacent particles, and the sec-
800 ond principal radius can be estimated from the distance between the Apollonius circle
801 and the particle contact.

With gravity ignored, the pressure difference across the liquid—ice interface $\Delta P = P_{nw} - P_l$ is determined by the Young-Laplace equation

$$-\frac{1}{y\sqrt{1+y'^2}} + \frac{y''}{(1+y'^2)^{3/2}} = \frac{\Delta P}{\gamma} = \mathcal{K} \tag{A1}$$

802 where the negative sign refers to a concave meniscus and the positive sign corresponds
803 to a convex one. Here we focus on the concave case.

The shape of the unduloid is complicated. As a result, the interface is often approximated as part of a toroidal surface (Fisher, 1926). In eq. (A1), we let

$$\frac{y''}{(1+y'^2)^{3/2}} = \frac{1}{r_1} \tag{A2}$$

$$\frac{1}{y\sqrt{1+y'^2}} = \frac{1}{r_2} \tag{A3}$$

804 where r_1 is the radius of curvature of the liquid bridge in the horizontal plane, and r_2
805 is the radius of curvature in the vertical plane. In other words, r_1 is the radius of the
806 poloidal circle, and r_2 is for the toroidal circle.

If the poloidal center in the horizontal plane is at (x_0, y_0), the relevant part of the circle is determined by

$$x = x_0 + r_1 \cos\beta, \quad y = y_0 - r_1 \sin\beta \tag{A4}$$

where $0 < \beta < \pi$ increases in a clockwise direction. The approximation automatically satisfies the curvature for r_1, while for r_2,

$$r_2 = \frac{y_0}{\sin\beta} - r_1 \tag{A5}$$

and for small arc segment, $\beta \approx \pi/2$, $r_2 \approx y_0 - r_1$. The mean curvature is reduced to

$$\mathcal{K} = \frac{1}{r_1} - \frac{1}{r_2}. \tag{A6}$$

To calculate r_1, we solve for the Apollonius circle touching two circles and one point. The test point must be within the truncated cone region formed with the common tangent line of the two spheres as its generatrix. If the test point is outside the truncated cone, no crevice ice can form even though a circle passing through the point can still be found.

Appendix B Undercooling caused by solute

B1 Common chloride salts

Salt in liquid water changes the activity of water, and the bulk equilibrium temperature shifts from T_m to T_m^* as

$$\ln a_w = \frac{\Delta H_{\text{fus}}}{R}\left(\frac{1}{T_m} - \frac{1}{T_m^*}\right). \tag{B1}$$

where $\Delta H_{\text{fus}} = 6.01\,\text{kJ/mol}$ is the molar enthalpy of fusion of water (Poling et al., 2001), and R is the gas constant. A similar relation also applies to the inhibited formation of methane hydrates in seawater. Many models exist to calculate the a_w for salts, and in relatively low concentrations, they predict similar result. We use the ZSR (Zdanovskii-Stokes-Robinson) equation (King, 1969) for its simplicity

$$m_s = \sum_i K_i a_w^i \tag{B2}$$

and the coefficients for three common chloride salts NaCl, KCl and $MgCl_2$ are summarized in Table B1. Note that in calculating the water activity, the salt concentration is usually in molality (moles of solute per one kilogram of water), while in calculating the undercooling, it is convenient to use molarity (moles of solute per one liter of solution). At low salt concentrations, these two values are close, but as more water freezes, the salinity of residual liquid increases, and the density can deviate from pure water significantly, so that conversion using a density model for salty water (e.g., Spivey et al., 2004) becomes necessary. In all the calculations, we limit the maximum concentration to their eutectic concentration.

Table B1. The polynomial coefficients for NaCl, KCl and $MgCl_2$.

solute	K_0	K_1	K_2	K_3	K_4	m_{eu} (mol/kg)
NaCl[a]	58.752 48	−187.819 97	272.113 77	−184.582 87	41.536 89	5.20[c]
KCl[a]	135.024 39	−475.357 98	697.384 95	−476.219 38	119.161 58	3.29[c]
$MgCl_2$[b]	11.505	−26.518	34.937	−19.829		2.79[d]

[a] Tang (1997)

[b] Kim and Seinfeld (1995)

[c] Bakker (2012)

[d] Altheide et al. (2009)

B2 Perchlorate salts

Unlike chloride salts, water activity models for perchlorate solutes are more complicated, so instead we used a polynomial fit between the freezing points and perchlorate concentrations reported by Pestova et al. (2005), with fixed end points $T(0) = 273.15\,\mathrm{K}$ and $T(m_{eu}) = T_{eu}$.

Figure 1.

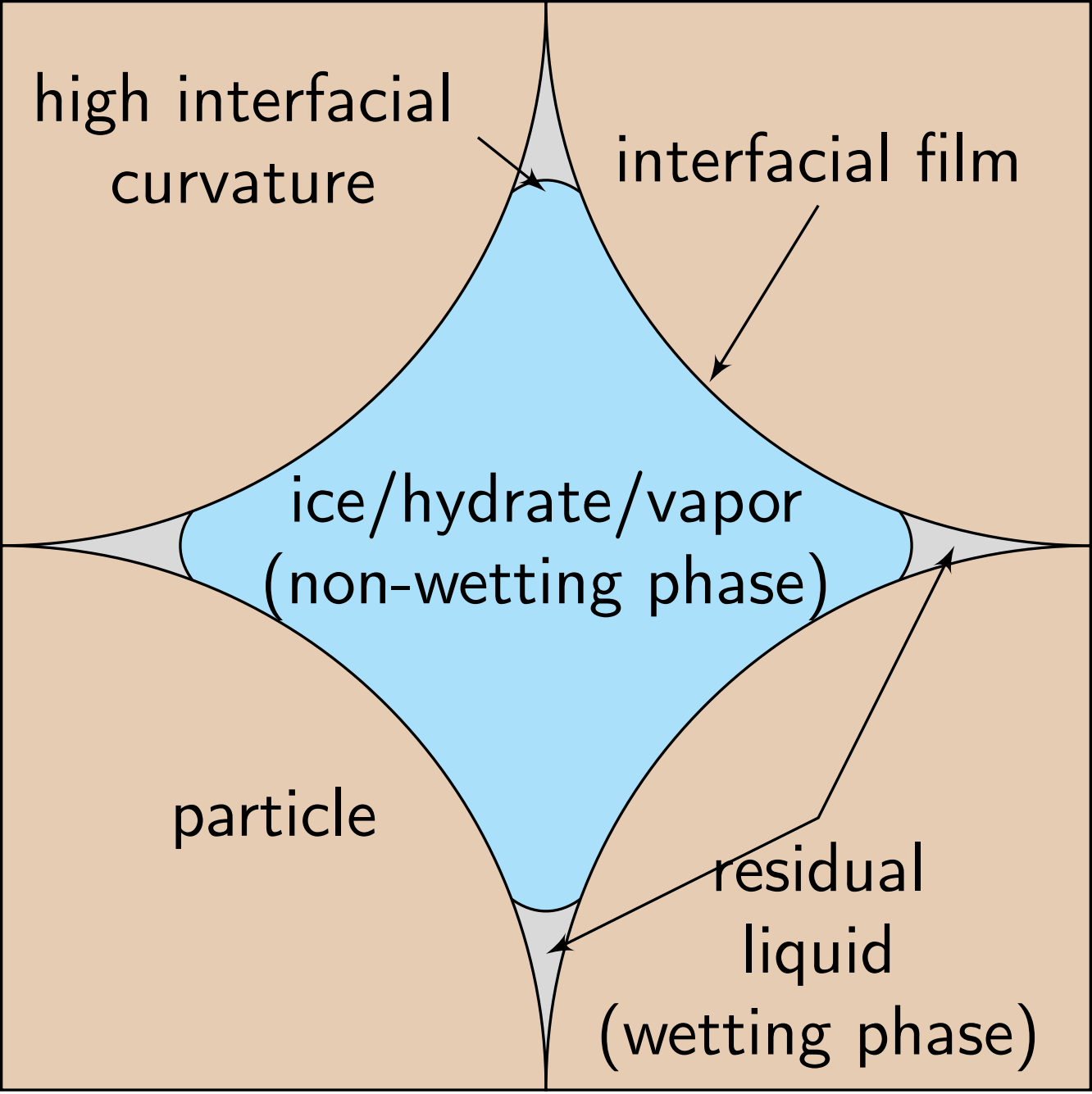
high interfacial
curvature
interfacial film
ice/hydrate/vapor
(non-wetting phase)
particle
residual
liquid
(wetting phase)

Figure 2.

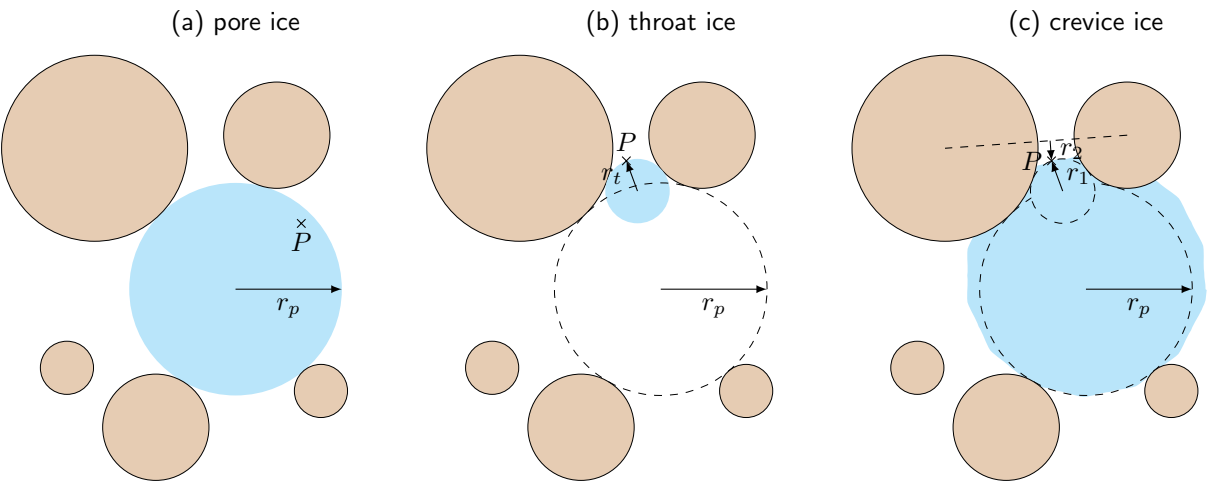
(a) pore ice
P
r_p
(b) throat ice
P
r_t
r_p
(c) crevice ice
P
r_2
r_1
r_p

Figure 3.

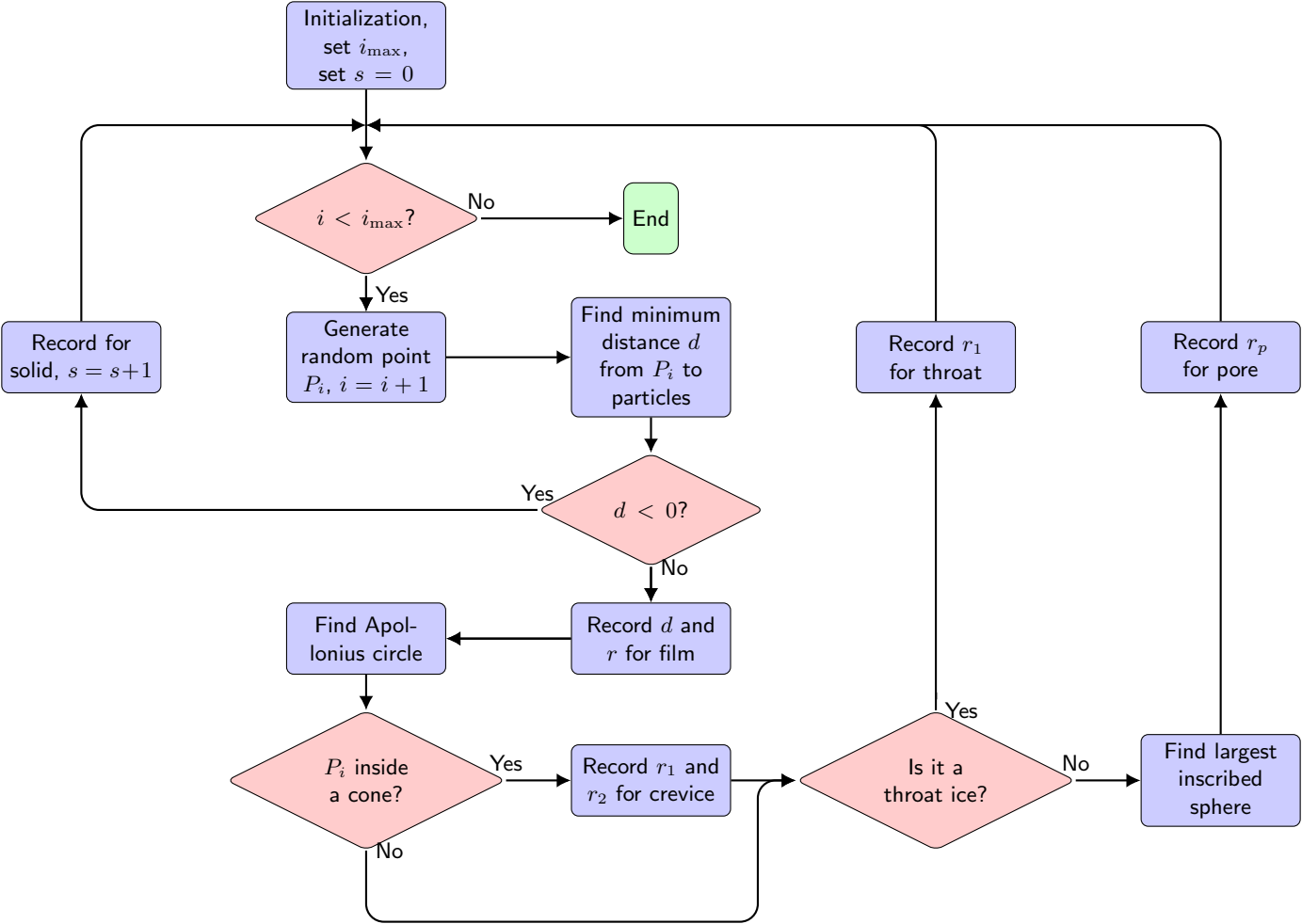
Initialization, set $i_{\max}$, set $s = 0$
$i < i_{\max}$?
No
End
Yes
Generate random point P_i, $i = i + 1$
Find minimum distance d from P_i to particles
Record for solid, $s = s+1$
Yes
$d < 0$?
No
Record d and r for film
Find Apollonius circle
P_i inside a cone?
Yes
Record r_1 and r_2 for crevice
No
Record r_1 for throat
Yes
Is it a throat ice?
No
Find largest inscribed sphere
Record r_p for pore

Figure 4.

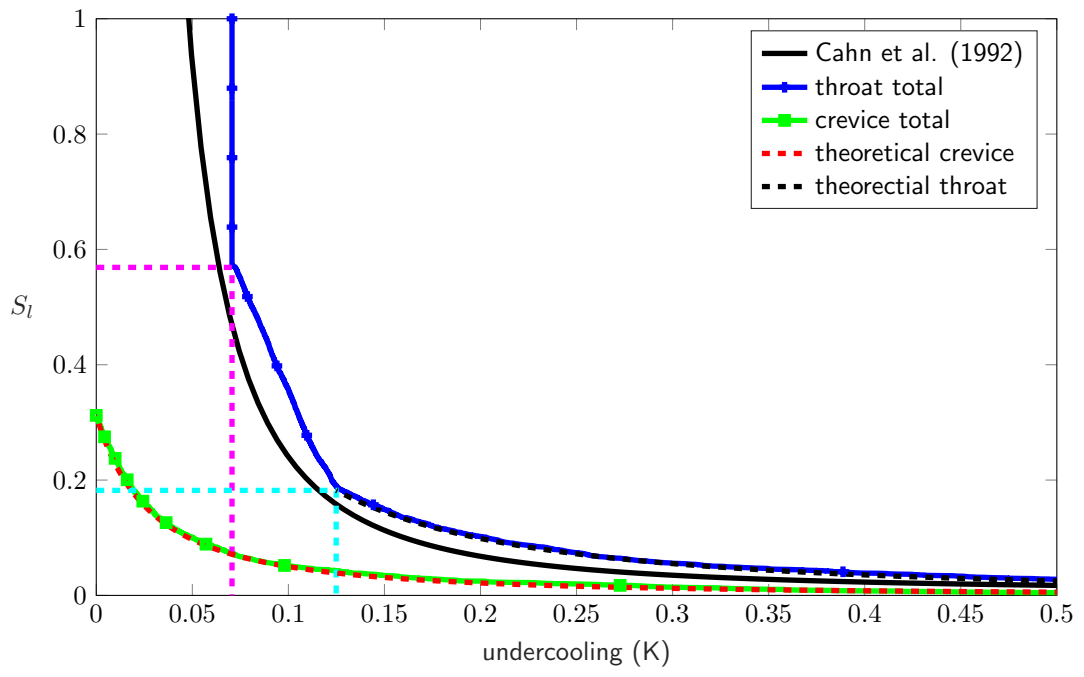
Cahn et al. (1992)
throat total
crevice total
theoretical crevice
theorectial throat
S_l
undercooling (K)
0
0.2
0.4
0.6
0.8
1
0
0.05
0.1
0.15
0.2
0.25
0.3
0.35
0.4
0.45
0.5

Figure 5a.

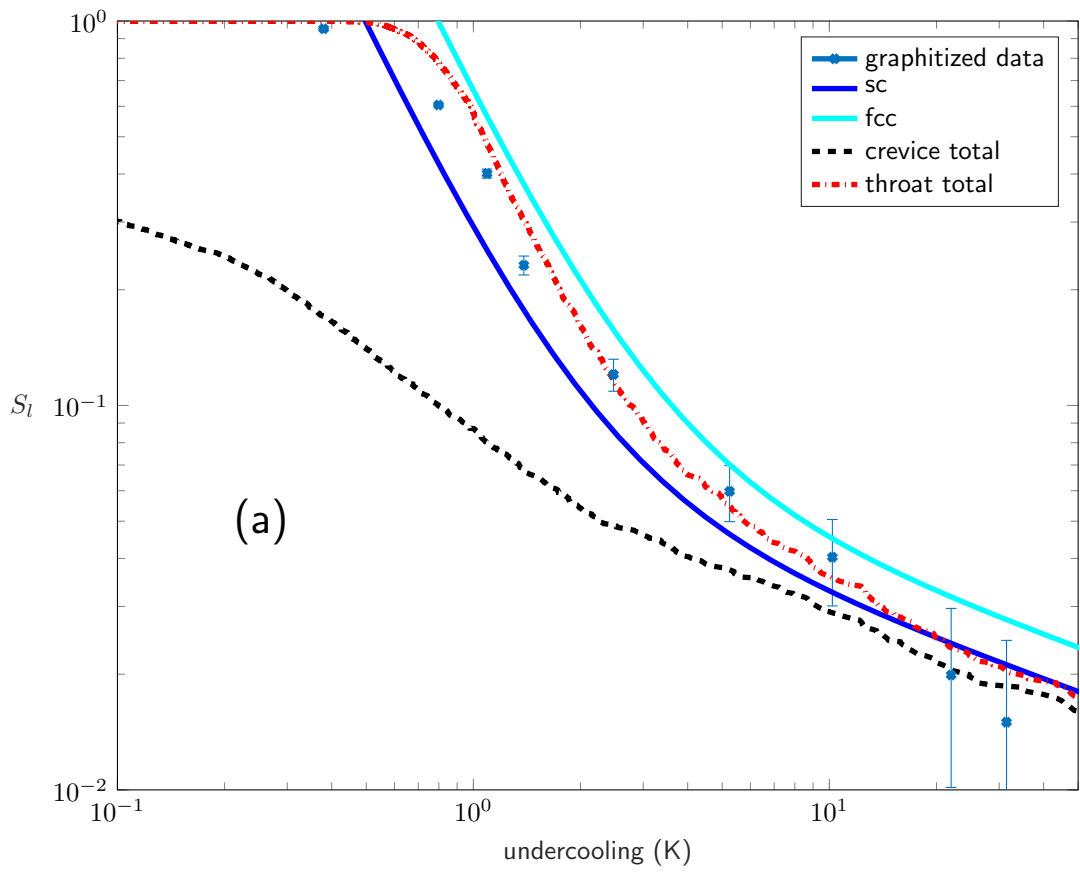
graphitized data
sc
fcc
crevice total
throat total
S_l
10^0
10^{-1}
10^{-2}
(a)
10^{-1}
10^0
10^1
undercooling (K)

Figure 5b.

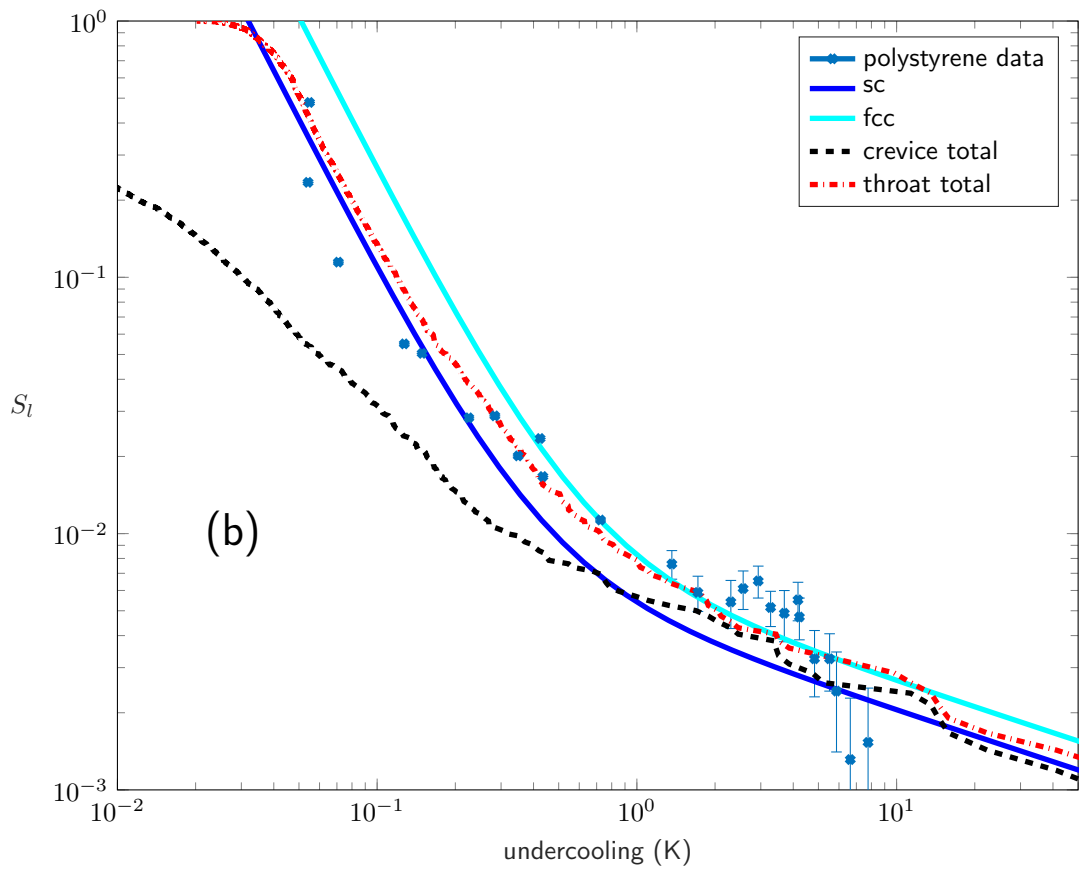
polystyrene data
sc
fcc
crevice total
throat total
(b)
S_l
undercooling (K)
10^0
10^{-1}
10^{-2}
10^{-3}
10^{-2}
10^{-1}
10^0
10^1

Figure 6.

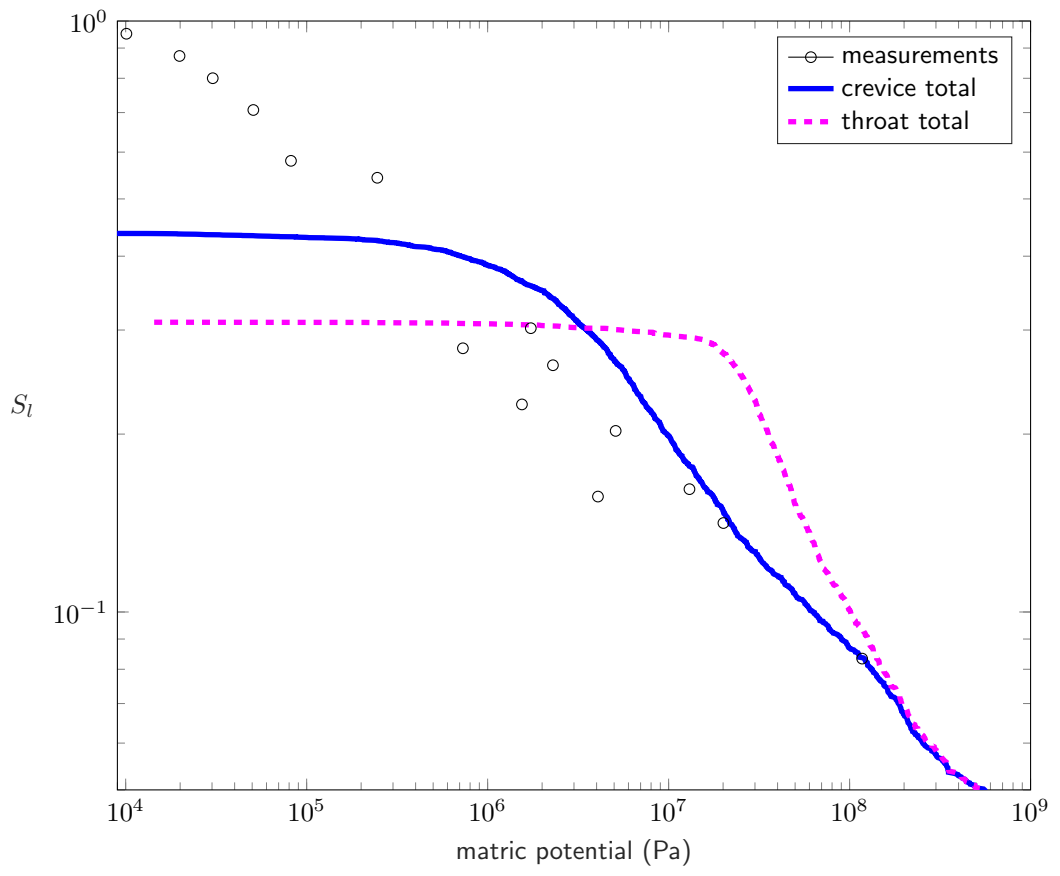
measurements
crevice total
throat total
10^0
10^{-1}
S_l
10^4
10^5
10^6
10^7
10^8
10^9
matric potential (Pa)

Figure 7a.

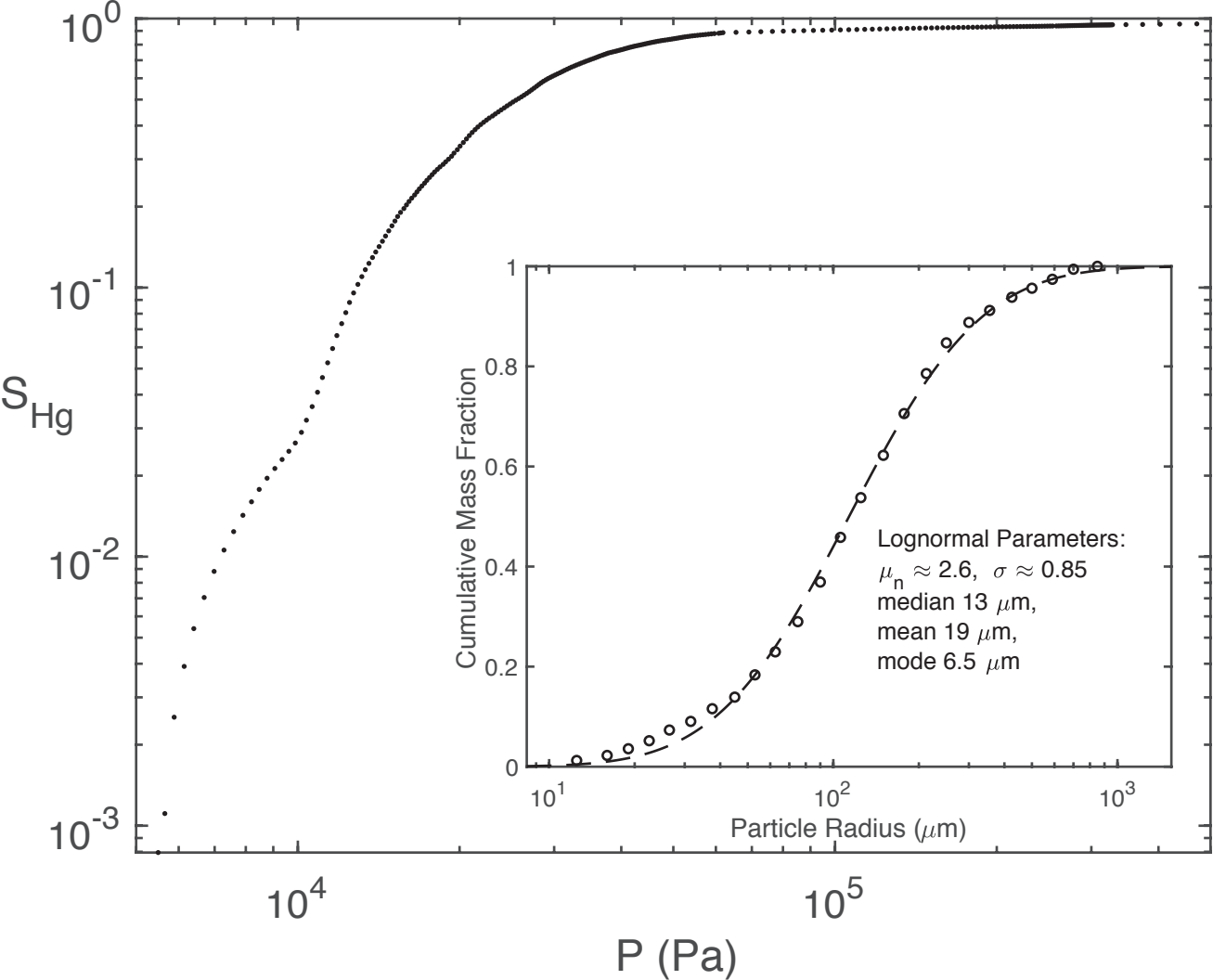
10^0
10^{-1}
10^{-2}
10^{-3}
S_{Hg}
10^4
10^5
P (Pa)
Cumulative Mass Fraction
0
0.2
0.4
0.6
0.8
1
10^1
10^2
10^3
Particle Radius (μm)
Lognormal Parameters:
$\mu_n \approx 2.6$, $\sigma \approx 0.85$
median 13 μm,
mean 19 μm,
mode 6.5 μm

Figure 7b.

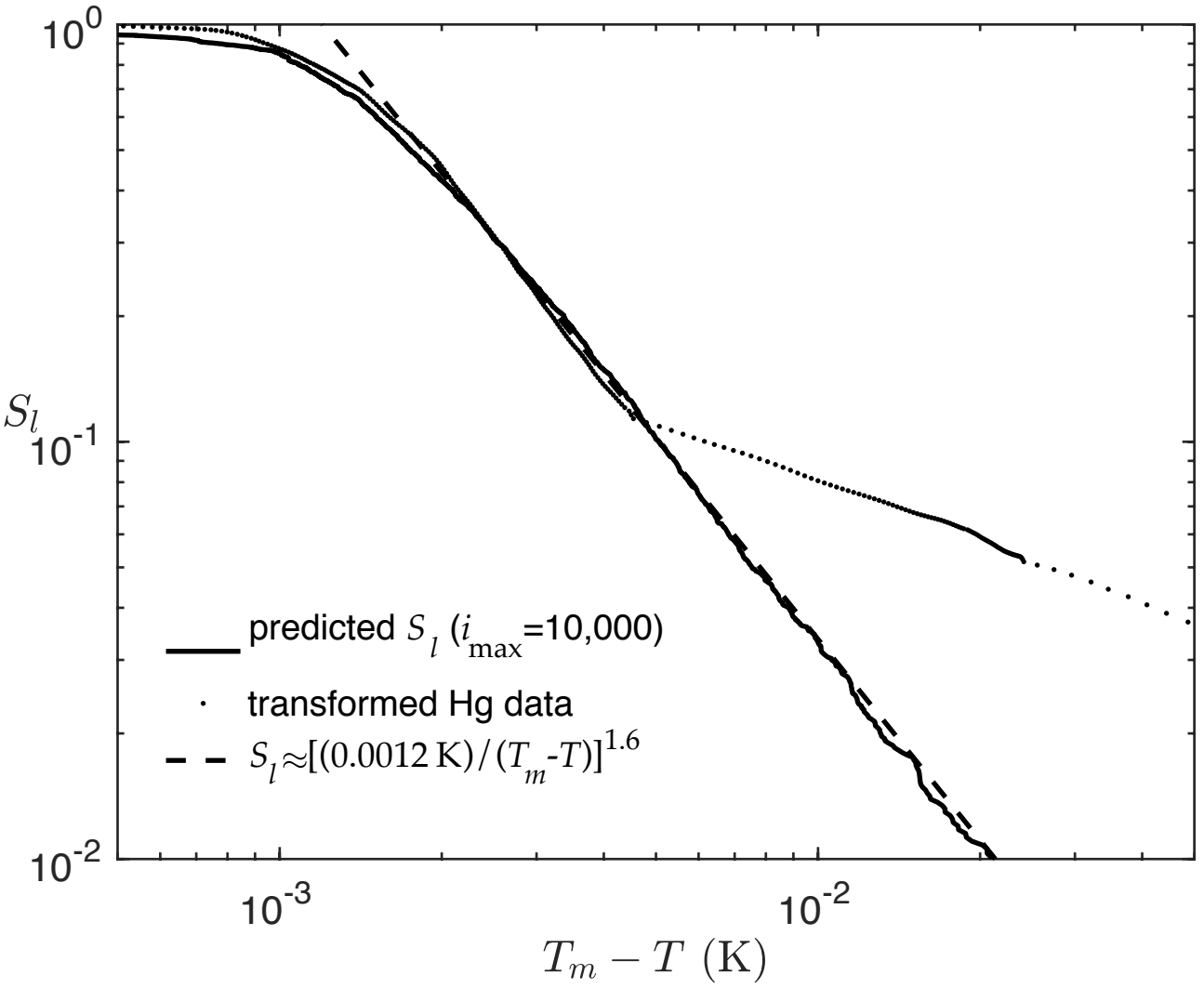
10^0
10^{-1}
10^{-2}
S_l
predicted S_l ($i_{\max}$=10,000)
transformed Hg data
$S_l \approx [(0.0012\,\mathrm{K})/(T_m\text{-}T)]^{1.6}$
10^{-3}
10^{-2}
$T_m - T$ (K)

Figure 8.

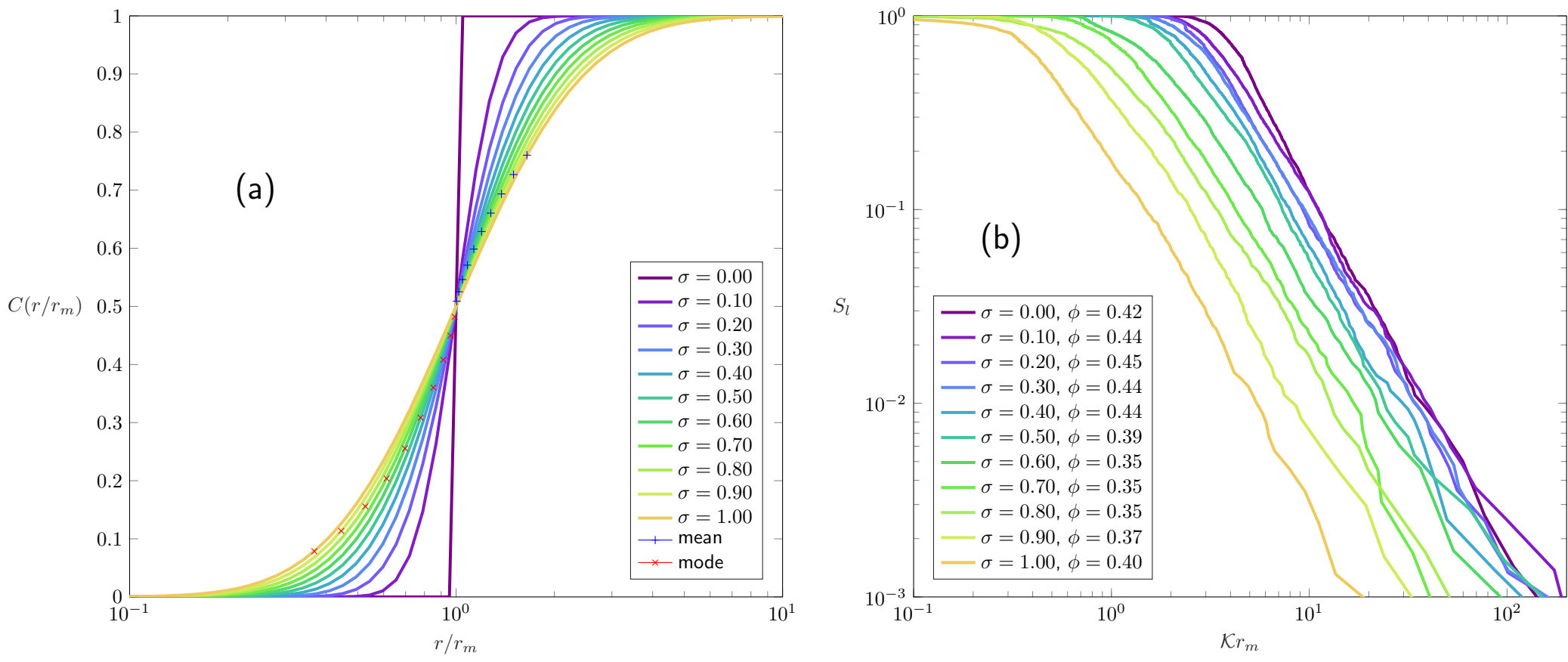
(a)
$C(r/r_m)$
r/r_m
10^{-1}
10^{0}
10^{1}
0
0.1
0.2
0.3
0.4
0.5
0.6
0.7
0.8
0.9
1
$\sigma = 0.00$
$\sigma = 0.10$
$\sigma = 0.20$
$\sigma = 0.30$
$\sigma = 0.40$
$\sigma = 0.50$
$\sigma = 0.60$
$\sigma = 0.70$
$\sigma = 0.80$
$\sigma = 0.90$
$\sigma = 1.00$
mean
mode
(b)
S_l
$\mathcal{K}r_m$
10^{0}
10^{-1}
10^{-2}
10^{-3}
10^{1}
10^{2}
$\sigma = 0.00,\ \phi = 0.42$
$\sigma = 0.10,\ \phi = 0.44$
$\sigma = 0.20,\ \phi = 0.45$
$\sigma = 0.30,\ \phi = 0.44$
$\sigma = 0.40,\ \phi = 0.44$
$\sigma = 0.50,\ \phi = 0.39$
$\sigma = 0.60,\ \phi = 0.35$
$\sigma = 0.70,\ \phi = 0.35$
$\sigma = 0.80,\ \phi = 0.35$
$\sigma = 0.90,\ \phi = 0.37$
$\sigma = 1.00,\ \phi = 0.40$

Figure 9.

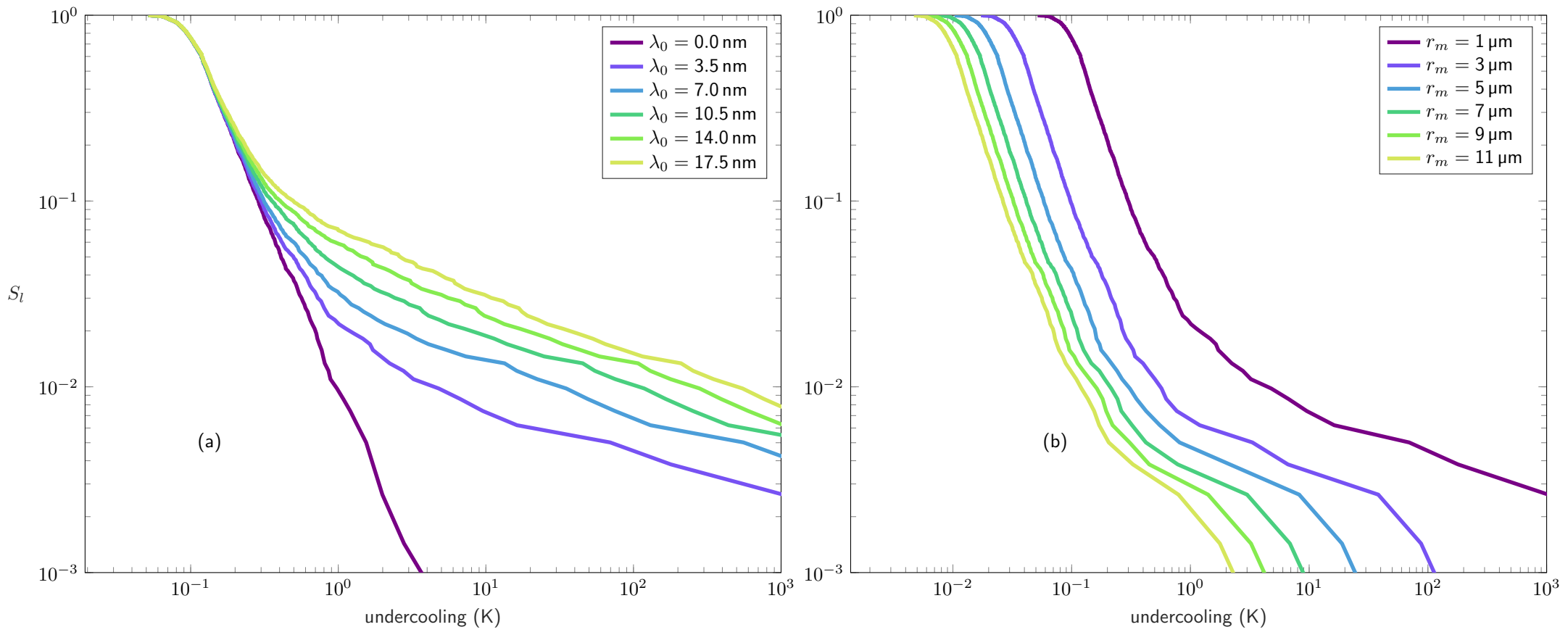
10^0
10^{-1}
10^{-2}
10^{-3}
S_l
(a)
$\lambda_0 = 0.0$ nm
$\lambda_0 = 3.5$ nm
$\lambda_0 = 7.0$ nm
$\lambda_0 = 10.5$ nm
$\lambda_0 = 14.0$ nm
$\lambda_0 = 17.5$ nm
10^{-1}
10^0
10^1
10^2
10^3
undercooling (K)
(b)
$r_m = 1$ µm
$r_m = 3$ µm
$r_m = 5$ µm
$r_m = 7$ µm
$r_m = 9$ µm
$r_m = 11$ µm
10^{-2}
10^{-1}
10^0
10^1
10^2
10^3
undercooling (K)

Figure 10.

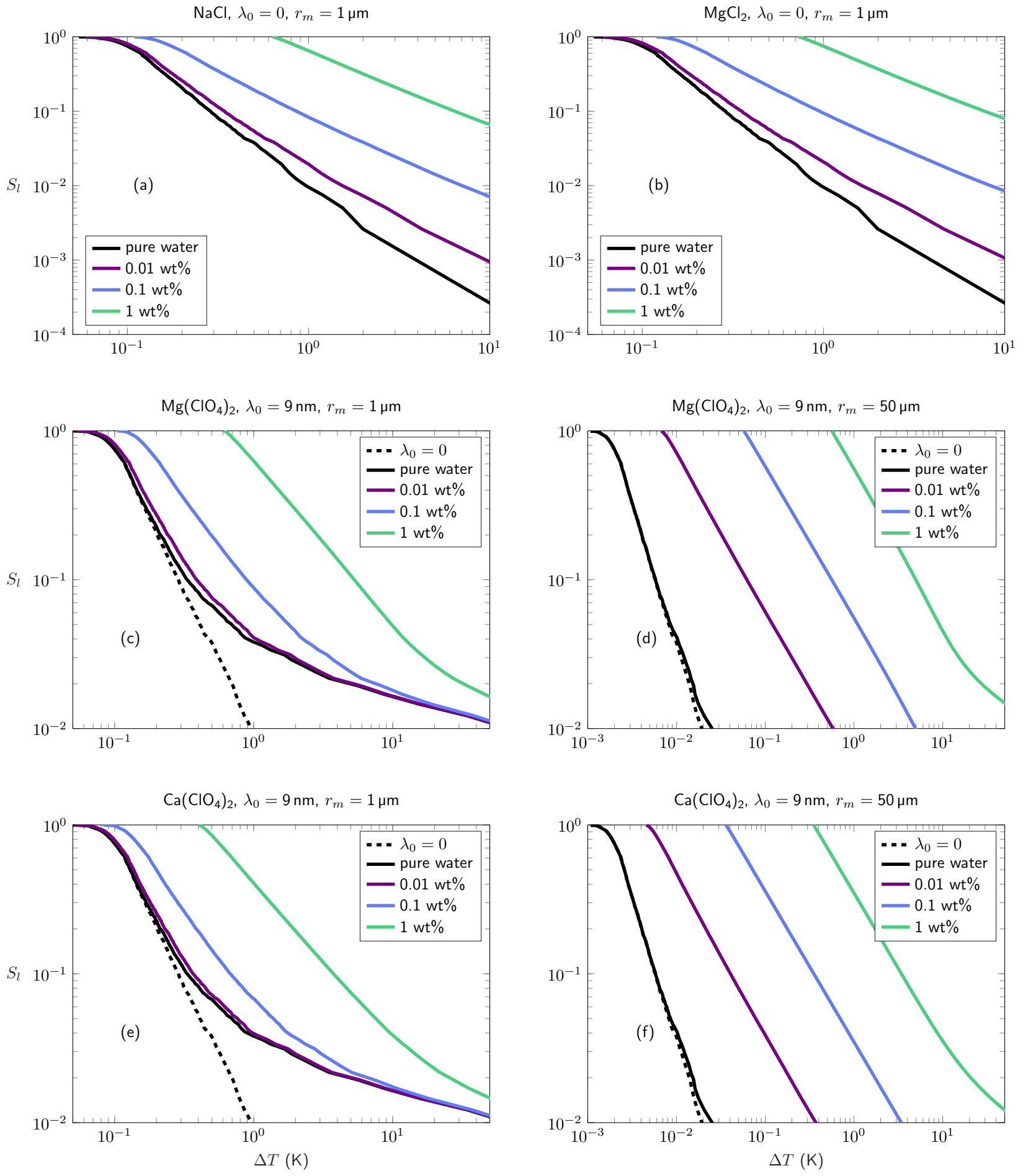
NaCl, $\lambda_0 = 0$, $r_m = 1\,\mu m$
$MgCl_2$, $\lambda_0 = 0$, $r_m = 1\,\mu m$
$Mg(ClO_4)_2$, $\lambda_0 = 9\,nm$, $r_m = 1\,\mu m$
$Mg(ClO_4)_2$, $\lambda_0 = 9\,nm$, $r_m = 50\,\mu m$
$Ca(ClO_4)_2$, $\lambda_0 = 9\,nm$, $r_m = 1\,\mu m$
$Ca(ClO_4)_2$, $\lambda_0 = 9\,nm$, $r_m = 50\,\mu m$
S_l
ΔT (K)
(a)
(b)
(c)
(d)
(e)
(f)
$\lambda_0 = 0$
pure water
0.01 wt%
0.1 wt%
1 wt%